Investigating secondary ice production in a deep convective cloud with a 3D bin microphysics model: Part I - Sensitivity study of microphysical processes representations

Pierre Grzegorczyk, Wolfram Wobrock, Antoine Canzi, Laurence Niquet, Frédéric Tridon, Céline Planche

Journal Pre-proof

Investigating secondary ice production in a deep convective cloud with a 3D bin microphysics model: Part I - Sensitivity study of microphysical processes representations

Pierre Grzegorczyk, Wolfram Wobrock, Antoine Canzi, Laurence Niquet, Frédéric Tridon, Céline Planche

PII: S0169-8095(24)00556-8

DOI: https://doi.org/10.1016/j.atmosres.2024.107774

Reference: ATMOS 107774

To appear in: *Atmospheric Research*

Received date: 26 July 2024

Revised date: 28 October 2024

Accepted date: 5 November 2024

Please cite this article as: P. Grzegorczyk, W. Wobrock, A. Canzi, et al., Investigating secondary ice production in a deep convective cloud with a 3D bin microphysics model: Part I - Sensitivity study of microphysical processes representations, *Atmospheric Research* (2024), https://doi.org/10.1016/j.atmosres.2024.107774

Investigating Secondary Ice Production in a Deep Convective Cloud with a 3D Bin Microphysics Model: Part I - Sensitivity study of Microphysical Processes Representations

Pierre Grzegorczyk[a,1,], Wolfram Wobrock[a], Antoine Canzi[a], Laurence Niquet[a], Frédéric Tridon[b,a], Céline Planche[a,c,2,]

[a] *Universite Clermont Auvergne, CNRS INSU, Laboratoire de Meteorologie Physique UMR 6016, F-63000, Clermont-Ferrand, France*

[b] *DIATI, Politecnico di Torino, Turin, Italy*

[c] *Institut Universitaire de France (IUF), France*

Abstract

Secondary ice production (SIP) is a crucial phenomenon for explaining the formation of ice crystal clouds, especially when addressing the discrepancies between observed ice crystal number concentrations and ice nucleating particles (INPs). In this study, we investigate parameterizations of three SIP processes (Hallett-Mossop, fragmentation of freezing drops, and fragmentation due to ice–ice collision) by simulating a deep convective cloud observed during the HAIC/HIWC campaign with the 3D bin microphysics scheme DESCAM (DEtailed SCAvening and

Email addresses: p.grzegorczyk@opgc.fr (Pierre Grzegorczyk), celine.planche@uca.fr (Céline Planche)

[1]Corresponding author

[2]Corresponding author

Microphysics model). The simulated mean cloud properties, including particle size distributions and ice crystal number concentration are compared with in situ probe observations obtained during the campaign. Simulation excluding SIP show a large underestimation of small ice crystals (< 1 mm diameter) for temperatures warmer than -30 °C. In our results, incorporating Hallett-Mossop and fragmentation due to ice–ice collision processes leads to ice crystal number concentrations close to observed values, thereby reducing discrepancies by two orders of magnitude. Our simulations also indicates that fragmentation of freezing drops affect minimally the properties of the cloud at its mature stage. Furthermore, we investigate the impact of fragments sizes resulting from SIP processes and show that the size of fragments generated from fragmentation due to ice–ice collision significantly influences the shape of ice particle size distribution. Employing various parameterizations of the ice crystal sticking efficiency reveals a notable impact on cloud properties. This study shows that SIP mechanisms are important and have to be considered for cold and mixed-phase clouds. However their parameterization lack reliability, highlighting the need for better quantifying these mechanisms. The companion paper, investigates the effects of SIP processes on the formation and the evolution of the deep convective system.

Keywords: Cloud microphysics, Convective cloud, Secondary ice production, Parameterization

1. Introduction

The ice phase of clouds exerts a significant influence on weather and climate by various ways. It impacts the development of clouds systems through condensation, melting and sublimation (Sawada and Iwasaki, 2007; Planche et al., 2014). On a global scale, 3/4 of surface precipitation originates from snowfall or melting processes (Heymsfield et al., 2020). Additionally, as highlighted by Matus and L'Ecuyer (2017) and Korolev et al. (2017), whether a

cloud is composed of water, ice, or both, affects the radiative energy balance and therefore the earth climate.

The observed disparities between the number of ice crystals and ice nucleating particles (INPs) is a major unknowns regarding the ice phase of clouds. While these inconsistencies have been recorded for a long time (e.g. Hallett et al., 1978; Hobbs et al., 1980; Hobbs and Rangno, 1985), they could be influenced by shattering effects on airborne in situ probes. Even if the shattering problem is currently fixed by improving in situ probes (Korolev et al., 2011), the discrepancies between INPs and ice crystal number concentration remain still observed (Kanji et al., 2017). This is particularly true in deep convective clouds, as demonstrated by Ladino et al. (2017), where a difference of 4 orders of magnitude was observed at -5 °C.

Therefore, secondary ice production (SIP) processes have been suggested as mechanisms that could explain the observed high concentrations of ice crystals. Six SIP mechanisms are mentioned in Korolev and Leisner (2020) to explain the discrepancies between INPs and ice crystals number concentration. In this study, we assessed the role of 3 SIP mechanisms: splintering during riming, fragmentation of freezing drops, and fragmentation due to ice-ice collisions.

Splintering during riming (hereafter called HM for Hallett-Mossop) occurs during riming of ice crystals. This process has been observed during various laboratory experiments in the 70-80's (e.g. Hallett and Mossop, 1974; Mossop, 1976; Choularton et al., 1978, 1980; Heymsfield and Mossop, 1984).

Fragmentation of freezing drops (hereafter mentioned as DS for drop shattering) is the second SIP mechanism examined in this study. It occurs during the freezing of a supercooled liquid drop, the ice shell extending toward the center of the drop, the internal pressure increases which could make the drop explode or crack. Such broken drops have been observed with in-situ

probes deployed onboard research aircrafts (see Lawson et al., 2015; Korolev et al., 2020), but also in ground based (e.g. in Lachapelle and Thériault, 2022) and in laboratory experiments (Lauber et al., 2018; Keinert et al., 2020).

Finally, we examine the fragmentation due to ice–ice collision process (hereafter mentioned as ice-ice breakup or BRK), which occurs during the mechanical fragmentation of colliding ice particles. Numerous observations indicate the susceptibility of ice crystals to break and produce fragments: Jiusto and Weickmann (1973) and Hobbs and Farber (1972) observed broken ice crystals during ground-based observations, Schwarzenboeck et al. (2009) observed similar broken ice particles via aircraft measurements, attributing them to natural fragmentation, and von Terzi et al. (2022) identified radar signatures which may come from the fragmentation of fragile aggregates. Despite that, only four laboratory studies dedicated to this process have been performed until now: Vardiman (1978), Griggs and Choularton (1986), Takahashi et al. (1995) and more recently Grzegorczyk et al. (2023).

The three other SIP mechanisms mentioned in Korolev and Leisner (2020) are not addressed in our study for the following several reasons. First, the fragmentation of ice crystals during thermal shock has limited observational support. Furthermore, thermal shock is occurring during HM and DS processes, which suggest that it could be included in both of these mechanisms. The fragmentation during sublimation is effective only in sub-saturated regions of the clouds such as on the cloud edges or anvils. Therefore, while the small fragments produced by sublimation may recirculate within saturated regions of the cloud, their impact is expected to be small. This assumption is supported by the study of Waman et al. (2022), that uses the parameterization of Deshmukh et al. (2022) in which fragmentation during sublimation is the least effective SIP mechanism. Finally, the activation of INPs in transient supersaturation is currently poorly

quantified from laboratory studies and therefore difficult to integrate into microphysical schemes.

In previous decades, bin or bulk microphysics models almost exclusively incorporated the Hallett-Mossop process, neglecting the existence of other SIP mechanisms, as noted by Field et al. (2017). However, this process alone is often not sufficient to explain the observed ice concentrations (see Farrington et al., 2016; Qu et al., 2018). Recently, a more pronounced attention has been directed towards secondary ice production, improving our knowledge about SIP mechanisms via the increasing number of studies laboratory experiments (e.g. Keinert et al., 2020; James et al., 2021; Grzegorczyk et al., 2023; Seidel et al., 2024) as well as in-situ observations (see Heymsfield and Willis, 2014; Korolev et al., 2020; Brechner et al., 2023; Lawson et al., 2023) making the implementation of the different SIP processes into models more feasible. Beyond ice crystal production, implementing SIP processes revealed other consequences such as changes in cloud convection (Dedekind et al., 2021; Karalis et al., 2022; Qu et al., 2022), precipitation (Hoarau et al., 2018; Dedekind et al., 2021; Georgakaki et al., 2022) or even radiative forcing (Young et al., 2019; Zhao and Liu, 2021; Waman et al., 2023).

However, inconsistent results exist among various modeling studies (e.g. between Waman et al. (2023) and Huang et al. (2022)). While Waman et al. (2023) shows an important effect of Hallett-Mossop process for a convective cloud, Huang et al. (2022) find the opposite. This demonstrate that the representation of the SIP processes remain uncertain.

The overall goal of this work is to investigate the representation of SIP processes as well as their impact on thermodynamical and microphysical properties of a deep convective cloud system observed in the tropics during HAIC/HIWC campaign (Fontaine et al., 2020; Hu et al., 2021) using DESCAM (DEtailed SCAvening and Microphysics model, Planche et al., 2010; Flossmann and Wobrock, 2010).

Using a bin microphysics model to study SIP processes has several advantages such as the sizes of the newly-formed ice fragments and particle size distributions that can evolve freely. Moreover, as highlighted by Arteaga et al. (2020), DESCAM model has demonstrated great reliability in its outcomes for cloud and precipitation features compared to WRF model (Weather Research and Forecasting; Skamarock et al., 2019) using bulk microphysics schemes (Thompson et al., 2008; Morrison et al., 2009) for an intense convective system over southern France. Furthermore, for this mid-latitude convective system an underestimated number of ice particles with $D < 1$ mm have been obtained (see Kagkara et al., 2020). This support the idea that SIP mechanisms should be included in DESCAM model to better reproduce the cloud microphysical properties.

This study, that is dedicated to evaluate the different representations available in the literature for HM, DS and BRK processes as well as identifying the most relevant parameterization for each of these SIP processes, is organized as follows: Section 2 describes succinctly DESCAM model. Section 3 is dedicated to the different parameterizations available to represent each of the studied SIP mechanisms. The observational data from HAIC/HIWC campaign used to constrain our simulations, modelling setup as well as the model results in a default configuration are presented in Section 4. The results of the different sensitivity experiments for SIP are presented in Section 5 (for single SIP process included) and Section 6 (for all SIP processes included) focusing on the features of ice crystal number concentrations, ice or liquid water contents and particle size distributions. Section 7 gives the key findings and conclusions which will be further used in the companion paper (Grzegorczyk et al., 2024, hereafter Part II) in order to understand the consequences of SIP mechanisms for the development of the deep convective cloud system.

2. DESCAM bin microphysics scheme

DESCAM is a bin microphysics scheme described in Flossmann and Wobrock (2010) coupled with the 3D non-hydrostatic and anelastic model of Clark et al. (1996) and Clark (2003). DESCAM is composed of six logarithmically spaced size distributions with mass doubling bins which represent interstitial aerosol particles (1 nm to 6 μm) , drops (2 μm to 13 mm), ice crystals (2 μm to around 10 cm) as well as aerosol mass within each drop and each ice crystal. Each distribution contains 39 mass bins. The rimed ice mass distribution (i.e., the mass of droplets freezing upon contact with an ice crystal) is constrained to the 27 largest bins of the ice crystal distribution (i.e. for ice crystals larger than 32 μm). This allows to define the rime fraction (ϕ) of each ice crystal bin as the ratio of the mass of rime to the total mass of the ice particle. Each bin is considered as a prognostic variable (i.e. 222 variables in total to describe aerosol particles and hydrometeors) which evolves spatially and temporally depending on microphysical processes and transport.

The warm microphysical processes considered are: nucleation of drops following the Köhler theory, vapor depositional growth, collision-coalescence, collisional breakup of drops according to Pruppacher et al. (1997) using laboratory experiments of Low and List (1982) and Beard and Ochs (1995). More details are available in Flossmann and Wobrock (2010).

Cold cloud microphysical processes considered are heterogeneous and homogeneous ice nucleation, vapor depositional growth, ice-droplet and ice-ice collisions. Heterogeneous ice nucleation is represented by the parameterization of Hiron and Flossmann (2015) while homogeneous ice nucleation follows the approach of Monier et al. (2006), which was developed based on Koop et al. (2000). Crystal growth and sublimation are calculated for spherical shaped particles. The size of unrimed ice crystals is calculated from the mass-diameter (m-D) power law

of Fontaine (2014). For rimed ice particles, similarly to Morrison and Grabowski (2010), the ”filling in” effect is considered by adjusting the m-D relationship based on the rime fraction. Particles that are sufficiently rimed are considered as graupel. In this case the m-D relationship of Heymsfield et al. (2018) is applied. The terminal fall velocity of each ice particle is determined as function of its size and rime fraction, following Heymsfield and Westbrook (2010).

As for drop-drop, ice-drop and ice-ice collisions are each considered by resolving the stochastic collection equation (SCE) using the numerical method of Bott (1998). Collision efficiencies used for ice-drop collision Kernels are based on different studies: Wang and Ji (2000) for unrimed ice crystals collecting drops, Cober and List (1993) for graupel-drop collision, and Lew et al. (1985) for the collection of crystals by large drops (> 100 μm). Ice-ice collisional kernels are based on studies of Böhm (1992a,b,c), which provide semi empirical solutions for the ice-ice collision efficiency. Sticking efficiency of colliding ice crystals is represented by two different parameterizations as described in Section 3.3.2.

Ice crystal formation via SIP processes is described in detail in Section 3 with a focus on HM, DS and BRK (i.e., the three SIP processes implemented in DESCAM as indicated in Section 1).

3. Parameterizations of secondary ice processes

3.1. Hallett-Mossop parameterizations

The physical mechanisms explaining Hallett-Mossop (HM) process remain unclear, as discussed in Korolev and Leisner (2020). Various explanations have been proposed such as the fragmentation of part of the drops during their symmetrical freezing (Choularton et al., 1978, 1980) or freezing of drops by glancing contact (Mossop, 1976). However, none of them was

confirmed as being the reason for production of ice splinters (called fragments hereafter).

Based on Heymsfield and Mossop (1984), the mean production rate of fragments by HM is function of the temperature (T) reaching a maximum of 200 fragments per mg of rime at -5 °C. With a similar temperature dependency, Hallett and Mossop (1974) observed a production of 300 and 700 fragments per mg of rime at -5 °C, which correspond to the mean and the maximum production of fragments, respectively. Furthermore, the literature also depicts the production rate of ice fragments as function of the number of drops larger than 25 μm (instead of rime mass), as presented in Mossop (1976), who observed a production rate of 1 fragment per 250 drops at -5 °C. Fig. 1 shows the rate of fragment production per mg of rime observed during all these different experiments (symbols) and the associated parameterizations. Solid lines represent the parameterizations based on the number of fragments per mg of rime, whereas dashed lines illustrate an equivalent number of fragments produced per 250 droplets, assuming 1 mg of rime consists of either 25 μm or 50 μm droplets. All these parameterizations have been implemented in DESCAM. Table 1 will summarize the setup of the different simulations performed in this study.

In that line, the loss of drops of mass m accreted by massive ice crystals of mass $m' > m$ is calculated by

$$\left(\frac{\partial n_D(m)}{\partial t}\right)_{riming} = -\int_m^\infty n_D(m) n_I(m') K_{riming}(m, m', \phi') dm' \tag{1}$$

where $n_D(m)$ and $n_I(m')$ are the drop and ice number distribution and $K_{riming}(m, m', \phi')$ the ice-drop collision kernel for ice crystals of rime fraction ϕ'. The number of fragments created by the Hallett-Mossop process is expressed by

$$\frac{\partial n_I(m_{frag})}{\partial t} = N_{HM} \cdot fct(T) \cdot \left(\frac{\partial n_D(m)}{\partial t}\right)_{riming} \tag{2}$$

with m_{frag} the mass of a fragments generated by accreted drops of mass m (refer to Equation 3), while $fct(T)$ is a temperature dependency function given by Cotton et al. (1986) based of the work of Hallett and Mossop (1974). N_{HM} is the maximum fragment production rate at -5°C in mg^{-1} (see Table. 1).

The mass or size of fragments resulting from Hallett-Mossop is rarely mentioned in previous studies. Some of them have nevertheless proposed the following hypothesis: a constant mass of 8.57×10^{-9} g (i.e. 30 μm) for Mansell and Ziegler (2013), 3.76×10^{-9} g (i.e. 20 μm) for Ziegler et al. (1986) while Khain and Lynn (2009) included all fragments into the first mass bin (2 μm in their study). In our study, the mass of the newly-formed ice splinters is assumed depending on the parent drop mass (based on Choularton et al. (1978) and Choularton et al. (1980) observations) and is given by

$$m_{frag}(m) = \min\left(0.015\times m, 1.71\times10^{-8}\right) \quad (3)$$

with m the mass of accreted droplets and $m_{frag}(m)$ the mass of the fragment in g.

In addition to assessing various parameterizations of the Hallett-Mossop process, we also examine the effect of ice fragment sizes on cloud properties by assigning all of them to the first bin of the ice crystal distribution, which corresponds to a diameter of 2.06 μm, as done in Khain and Lynn (2009). All simulations performed to assess the Hallett-Mossop (HM) process are listed in Table 1.

Figure 1: Ice fragment production rate for Hallett-Mossop process as a function of the temperature obtained by the laboratory experiments of Hallett and Mossop (1974) and Heymsfield and Mossop (1984) ('+' symbols). Solid lines represent the parameterizations deduced from these two

experiments according to rime mass while dashed lines show the fragment number per mg of rime equivalent to fragment number per frozen drop from Mossop (1976) for two drop sizes.

3.2. Drop shattering (or Fragmentation of Freezing Drops)

The examination conducted by Korolev and Leisner (2020) show that a large number of laboratory investigations have been conducted to explore the phenomenon of drop shattering (DS). These studies reveal that a drop has the capacity to generate fragments as a result of freezing upon contact with an ice crystal, an ice nucleating particle (INP), or spontaneously during immersion freezing. Based on numerous of these laboratory studies performed in 1970's, Phillips et al. (2018) developed a parameterization indicating a maximum fragment production rate at $-15^{\circ}\mathrm{C}$. Recent laboratory investigations (Keinert et al., 2020; Lauber et al., 2018) have demonstrated that the rate of fragment production can vary significantly depending on water composition, the presence of airflow being dry or moist. Therefore, uncertainties still remain regarding the number of fragments emitted via DS. Furthermore, Phillips et al. (2018) and James et al. (2021) identified another SIP mechanism which occurs when a large supercooled drop splashes on a more massive ice particle (see Section 3.2.1).

In our study, we consider that DS occurs after collision of supercooled drops with less massive ice crystals as well as after heterogeneous ice nucleation. The rate of frozen drops available to trigger DS is thus given by:

$$\left(\frac{\partial n_D(m)}{\partial t}\right)_{freez} = -\left[\int_0^m n_D(m) n_I(m') K(m,m',\phi) dm'\right]_{collection} + \left[\frac{\partial n_D(m)}{\partial t}\right]_{immersion}. \quad (4)$$

From this drop freezing rate, the total number of ice fragments is expressed by

$$\frac{\partial n_I(m_{frag})}{\partial t} = N_{DS}(m,T) \cdot \left(\frac{\partial n_D(m)}{\partial t}\right)_{freez} \quad (5)$$

with m_{frag} the mass of the fragments and $N_{DS}(m,T)$ the number of fragments per frozen drop which can be determined from the three different parameterizations : Phillips et al. (2018); Lauber et al. (2021); Sullivan et al. (2018) which are described in details in the following sections.

3.2.1. Parameterization of Phillips et al. (2018)

Phillips et al. (2018) (hereafter P18) proposed a parameterization to describe the number of fragments generated during drop shattering based on several laboratory studies mostly performed in 70's. First, collisions of drops with a less massive ice particle are referenced as 'mode 1' and result in the generation of two types of fragment ($N_{DS,1}^{small}$ and $N_{DS,1}^{big}$ for small and large fragments, respectively). Secondly, collision of drops with more massive ice particles are referenced as 'mode 2'.

The total number of fragments per drop formed via the 'mode 1' is expressed by

$$N_{DS,1} = F(D)\Omega(T)\left[\frac{\zeta\eta^2}{(T-T_0)^2+\eta^2}+\beta T\right] \tag{6}$$

where $\Omega(T)$ and $F(D)$ are two thresholds functions used to activate smoothly DS process between -3 to -6°C and for drop size from D = 50 to 60 μm. T_0, β, ζ and η are fitted parameters (see Phillips et al., 2018) which depend on drop size (D).

The small fragments are assumed to have a size of 10 μm, and their quantity is calculated by $N_{DS,1}^{small} = N_{DS,1} - N_{DS,1}^{big}$. The number of large fragments formed via the 'mode 1' is expressed by

$$N_{DS,1}^{big} = \min\left\{F(D)\Omega(T)\left[\frac{\zeta_B\eta_B^2}{(T-T_{B,0})^2+\eta_B^2}+\beta_B T\right], N_{DS,1}\right\}. \tag{7}$$

where the parameters are the same than for Eq. 6 but for large fragments (which are defined by the index B). The mass of large fragments is assumed to be 1/2.5 times the mass of the initial drop (i.e.

large fragments are coming from the total disruption of the drop which is assumed to happened in 2 or 3 parts).

The black line of Fig. 2 represents the total number of fragments produced by 'mode 1' according to P18 as a function of the temperature (T) and for three different drop sizes (D). Note that N_{DS} of Eq. 5 is considered to be equal to $N_{DS,1}$ when using P18 parameterization.

The mode 2 proposed in P18 for DS process corresponds to splash events occurring when drops (with $D > 150$ μm) collide with more massive ice crystals, resulting in the formation of small drops and ice fragments. Its production of secondary ice crystal is calculated using Eq. 1 but applying a threshold for the drop size (since mode 2 considered only for drops larger than 150 μm).

The number of ice fragments formed via mode 2 is expressed by

$$N_{DS,2} = 3\Phi \cdot [1 - f(T)] \cdot \max(DE - DE_{crit}, 0) \quad (8)$$

with $DE = \frac{K_0}{\sigma\pi D^2}$ the ratio between the collision kinetic energy (K_0) and the drop surface tension ($\sigma\pi D^2$), DE_{crit} = 0.2 is the threshold for the onset of drop splashing, $f(T)$ the freezing fraction of the incident drop which depends on temperature. Φ represent the fraction of frozen fragments and is set to 0.3 based on the experiments of James et al. (2021). Drop and ice fragment are supposed to have the mass $m_{frag}(m) = 0.001 \times m$ depending on the drop mass m as mentioned in P18. The parameterization of this mode is based on a limited number of laboratory experiments, implying a more uncertain representation than for the mode 1. Nevertheless, mode 2 is considered in all the simulations performed in this study when the parameterization of P18 is used (other parameterizations used in this study exclusively address mode 1). A detailed sensitivity study of mode 2 parameters is not discussed here but can be found in James et al. (2021).

3.2.2. Parameterization of Lauber et al. (2021)

Lauber et al. (2018) investigated drop shattering by levitating drops in stagnant air and identified various types of fragmentation, including breakup, cracking, jetting, and bubble bursts. The same experiment was performed by Keinert et al. (2020) (hereafter K20) who show that introducing airflow around the freezing drops increases the frequency of shattering events. Note that P18 parameterization is based on experiments performed in non stagnant air conditions. Furthermore, K20 also found that drop shattering also occurs at warm temperature (around $-2.5^{\circ}\mathrm{C}$) which is in contrast to P18 parameterization for mode 1 in which shattering is active for $T < -3^{\circ}\mathrm{C}$. Lauber et al. (2021) (hereafter L21) proposed a parameterization for the maximum number of fragments generated by drop shattering based on the shattering probability of K20 and the number of fragments found in Lauber et al. (2018) for temperature close to $0^{\circ}\mathrm{C}$.

This parameterization for the maximum number of fragments is expressed as:

$$N_{DS}^{tot}(D) = N_{DS}(D) \cdot P_{DS}(D) \tag{9}$$

with $N_{DS}^{tot}(D)$ the number of fragments which depends on the probability of droplet fragmentation $P_{DS}(D) = 4.4\times10^{6} D^{2}$ and on the maximum number of fragments per shattering event $N_{DS}(D) = 9.4\times10^{6} D$ which is based on the observations in Lauber et al. (2018) where D is the droplet diameter in m. However, L21 parameterization was developed for temperature next to the melting layer (i.e. $T > -3^{\circ}\mathrm{C}$) and needs to be adapted for colder temperatures.

We therefore propose to introduce the temperature dependency of shattering probability $P_{DS}(T)$ based on observations of K20 for 300 μm drops:

$$\begin{cases} P_{DS}(T) = P_{max} \cdot \exp\left(-\dfrac{(T+13.5)^2}{(2\sigma^2)}\right) & \text{(for T<-5°C)} \\ P_{DS}(T) = 0.4 \text{ (for -5°C < T < -1°C)} \\ P_{DS}(T) = -0.4 \cdot T \text{ (for T >-1°C)} \end{cases} \quad (10)$$

with σ = 4 and P_{max} = 0.9 which are derived from the temperature dependency of K20 experiments and T the temperature in °C. DS is activated linearly from 0°C to reach the values mentioned in L21 for -1°C.

However, as the original expression of L21 is given for T > -3°C and gives $P_{DS}(D = 300\mu m)$ = 0.4 and that at such temperature $P_{DS}(T)$ = 0.4, Eq. 9 need to be normalized by 0.4 when introducing $P_{DS}(T)$. The modified maximum number of L21 used for Eq. 5 becomes

$$N_{DS}^{tot}(D,T) = N_{DS}(D) \cdot \max\left(\frac{P_{DS}(T)}{0.4} \times P_{DS}(D), 1\right). \quad (11)$$

Fig. 2 shows that as the parameterization of P18 becomes active for T < -3°C and therefore that L21 parameterization gives much more fragments at warm temperatures.

As L21 developed their parameterization for DS process considering the maximum production of fragments, its implementation within DESCAM model will not reflect realistic ice concentrations formed by DS (see Section 5). However, it will serve to estimate the maximum order of magnitude of ice crystal concentrations reachable through DS process.

3.2.3. Parameterization of Sullivan et al. (2018)

Based on levitation experiments (Leisner et al., 2014; Lauber et al., 2018), Sullivan et al. (2018) (hereafter S18) proposed a parameterization for the number of fragments produced by DS process as a function of temperature (T) and drop size (D).

The number of ice splinters produced by the DS process according to S18 is expressed by

$$N_{DS}(D,T) = \frac{\alpha_{DS} P_{DS}(T)}{1+\exp[-\beta_{DS}(D-\gamma_{DS})]}. \quad (12)$$

The probability of shattering for a given temperature is defined by $P_{DS}(T) = 0.2 \cdot N(258K, 10K)$ with N the Gaussian probability distribution function centered at 258K. α_{DS}, γ_{DS} and β_{DS} are three constants which are equal to 10, 500 and -0.016 respectively.

As showed in Fig. 2, S18 parameterization predicts significantly fewer fragments than the one of P18 with up to 2 orders of magnitude difference for 0.1 mm drops next to $-15^{\circ}C$. This gap can be due to the different experimental conditions under which each parameterization is established. Indeed, S18 is based on levitation experiments conducted in still air, while P18 exclude experiments involving stationary drops.

3.2.4. Parameterization of Lawson et al. (2015)

Lawson et al. (2015) propose a relationship to link the number of ice fragments to the number of frozen drops (mentioned L15 hereafter). This relationship was established by simulating an air parcel using a bin microphysics model and fitting the fragmentation rate to observed drop and ice particle size distributions derived from aircraft observations. The following expression was obtained when the simulation matched the observations in terms of ice development and liquid water depletion. Consequently, the number of fragments per frozen drop is expressed by

$$N_{DS}^{L15}(D) = 2.5 \times 10^{11} D^4 \quad (13)$$

with D the drop diameter in μm. However, contrary to laboratory studies, this relation is based on an indirect observation of the DS process by linking frozen drops to fragment production.

Therefore, it cannot be asserted that all of these fragments are produced only by DS mechanism. Consequently, this relationship remain empirical and may encompass other secondary ice production mechanisms. In comparison to the other parameterizations L15 results in the largest number of fragments produced for drops of 2 mm diameter. Indeed, this relation is strongly sensitive to drop size due to the term D^4 in Eq. 13.

Figure 2: Number of ice fragments produced per drop during Drop shattering (DS) as a function of temperature for the parameterizations tested in our study: Phillips et al. (2018) (mode 1), Sullivan et al. (2018), Lauber et al. (2021) considering a temperature dependency based on the laboratory experiments of K20, and Lawson et al. (2015) for drop diameters of 0.1 mm (a), 0.5 mm (b), and 2 mm (c).

3.3. Ice-ice collisions

This section is dedicated to the processes that occurred during ice-ice collisions. Ice crystals can break due to mechanical forces arising from collisions and resulting in SIP. However, ice crystals can also stick together and form aggregates. The different parameterizations used in DESCAM to describe ice-ice breakup (BRK) or aggregation via sticking efficiency are detailed in the following two sections.

3.3.1. Ice-ice collision breakup

The theoretical parameterization proposed by Phillips et al. (2017) (hereafter P17) based on the physics of collisions is extensively employed in cloud models (e.g. Zhao et al., 2021; Sotiropoulou et al., 2021a; Waman et al., 2022; Patade et al., 2022; Huang et al., 2022). However,

several of the used parameters employed (A_M, C, γ, see Eq. 16) rely on only the laboratory studies of Vardiman (1978) and Takahashi et al. (1995), introducing uncertainties in the fragment number produced by BRK process. Additional laboratory studies (such as Grzegorczyk et al., 2023) are essential for refining these parameters. In this framework, our study proposes an alternative parameterization for the BRK process which is based on the theory of P17 but using the results of Grzegorczyk et al. (2023).

The BRK process is represented in DESCAM by the mass gain or loss in each bin of the crystal mass distribution function $g_I(m)$ analogously to the drop breakup equation (see Pruppacher et al., 1997, p. 647) with

$$\frac{\partial g_I(m)}{\partial t} = \overbrace{\int_0^{\infty}\int_0^{m''} n_I(m')n_I(m'')K(m',m'',\phi',\phi'')(1-E_s)mN_{frag}(m;m',m'')dm'dm''}^{\text{gain of mass from fragments of mass } m} - \underbrace{\int_m^{\infty} n_I(m)n_I(m')K(m,m',\phi,\phi')(1-E_s)\int_0^{m} N_{frag}(m'';m,m')m''dm''dm'}_{\text{loss of mass due to fragmentation of particle of mass } m}. \quad (14)$$

The first term expresses the mass gain of fragments of mass m that comes from the collision of ice particles of mass m' with other ice particles of mass m''. The second term expresses the loss of crystals of mass m which is due to the fragmentation induced by the collision with mass m'. The number of collisions per second is determined by the ice-ice collision kernels $K(m,m',\phi,\phi')$. We assume that only crystals which are not sticking together can break and create ice fragments (as expressed by the term $(1-E_s)$ in Eq. 14) and that the slowest falling ice crystal is fragmented by the one which is falling into it (as given in the experiments of Grzegorczyk et al., 2023). $N_{BRK}(m'';m',m)$ which is the number of fragments of mass m'' generated by the fragmentation of ice crystal of mass m due to the collision with m' is expressed by

$$N_{BRK}(m'';m',m) = N_{BRK}^{tot}(m,m') \cdot P(m,m'') \quad (15)$$

with $P(m,m'')$ the distribution function for fragment of mass m'' generated by an ice particle of mass m and $N_{BRK}^{tot}(m,m')$ the total number of fragments expressed from P17 theory:

$$N_{BRK}^{tot}(m,m') = \alpha(m,\phi)A_M(T,\phi)\left(1-\exp\left(-\frac{C(\phi)K_0(m,m',\phi,\phi')}{\alpha(m,\phi)A_M(T,\phi)}\right)^{\gamma}\right). \quad (16)$$

$\alpha(m,\phi)$ is the surface area of the smallest ice crystal in m^2, $A_M(T,\phi)$ the total number of breakable asperities of the ice particle per area in m^{-2}, $C(\phi)$ the fragility asperity coefficient in J^{-1}, $K_0(m,m',\phi,\phi')$ the collision kinetic energy (CKE) and γ the shape parameter. In our study, we performed simulation with the original $A_M(T,\phi)$, $C(\phi)$ and γ parameters (see Table 1 of Phillips et al., 2017) and simulations with the analogous parameters derived from Grzegorczyk et al. (2023) (given in Table. 2).

Grzegorczyk et al. (2023) (hereafter G23) determined the values of $A_M(T,\phi)$, $C(\phi)$ and γ parameters based on 3 different types of collisions. Values from graupel-snowflake collisions are used for the breakup of non/slightly rimed particles ($\phi < 0.5$) whereas for rimed particles, values from the two other collisions experiments (i.e. graupel-graupel and graupel-graupel with dendrites) are interpolated according to supersaturation with respect to ice (S_i) (see Table. 2). This S_i dependency lies in the fact that collisions involving bare graupels are conducted in an environment without any vapor depositional growth (supposed to be close to ice saturation) while graupel-graupel with dendrites collisions are performed under highly supersaturated conditions (S_i = 0.23).

Collision type	$A_M(-15^{\circ}\mathrm{C},\phi)$ (m^{-2})	C (J^{-1})	γ
Unrimed particle ($\phi < 0.5$)	4.75×10^7	1.0×10^8	0.78

Rimed particle ($\phi > 0.5$)	$1.6 \times 10^{6} \exp(14.5 S_i + 15.67)$	$9.7 \times 10^{5} \exp(20.15 S_i + 13.78)$	$S_i + 0.55$

Table 2: Parameters used for the parameterization of Phillips et al. (2017) based on the laboratory study of G23 at T = -15°C. 'Unrimed particle' corresponds to graupel-snowflake collisions whereas the 'rimed particle' corresponds to the interpolation of the properties found for graupel-graupel collsions as well as graupel-graupel with dendrite collisions.

For unrimed and rimed ice crystals, the dependency of $A_M(T,\phi)$ to temperature is considered. Takahashi et al. (1995) described the influence of the temperature on the number of fragments produced at maximum CKE. In that case, the total number of fragments can be expressed by $N_{BRK}^{tot}(m,m') = \alpha(m,\phi) A_M(T,\phi)$ with the probability to break all asperities which is 1 due to a high CKE. Based on that, we used the following temperature dependency proposed by P17:

$$A_M(T,\phi) = A_M(-15^{\circ}\mathrm{C},\phi)\left(\frac{1}{3} + \max\left(0., \frac{2}{3} - \frac{1}{9} \times |15.0 + T|\right)\right) \quad (17)$$

with T the temperature in °C. Eq. 17 therefore represents a triangular temperature dependency on the number of breakable asperities found by Takahashi et al. (1995) with a maximum at -15°C .

Fig. 3 illustrates the two different parameterizations representing the number of fragments generated during the breakup of rimed and unrimed ice crystals as a function of the CKE. In Fig. 3a, close to ice saturation (e.g. S_i = 0.04), the number of ice fragments derived from G23 is close to the original P17 parameterization (see black dashed line) while for high ice supersaturation (e.g. S_i = 0.2), the number of fragments increases significantly, diverging from P17. As visible from

Fig. 3b, P17 parameterization is strongly dependent on the rime fraction as emphasized by Karalis et al. (2022). Thus, the original version of P17 parameterization gives less ice fragments than using coefficient derived from G23 for unrimed ice crystals ($\phi = 0$). However, G23 is closer to P17 for planar crystals or dendrites with ϕ = 0.5.

Regarding the fragments properties, P17 assumed that the mass of fragments is 10^{-6} times the mass of the parent particle for hail collisions (associated to rimed ice crystals of D > 0.5 cm for DESCAM) and 10^{-3} for other collisions. We also use the fragment mass distribution function $P(m, m'')$ analogous to the fragment size probability distribution of G23 to describe the population of fragments:

$$P(m, m'') = \frac{1}{\sigma(m,\phi)\sqrt{2\pi}} \cdot \exp\left(\frac{\ln(m'') - \mu(m,\phi)}{2\sigma(m,\phi)^2} \right) \Delta m \tag{18}$$

with Δm the mass bin width (which is doubling in DESCAM). Since G23 showed two fragment size distributions corresponding to different parent particles (4 mm graupel or 10 mm snowflake) we hypothesized that the distribution mode $\mu(m,\phi)$ and standard deviation $\sigma(m,\phi)$ are dependent of the size of the parent ice particle. Consequently, for all collision types, we employed a linear interpolation for adjusting $\mu(m,\phi)$ and $\sigma(m,\phi)$ depending on the size of the parent particle of mass m:

$$\begin{cases} \mu(m,\phi) = \min\left(3.95 \cdot D(m,\phi) - 15.4, -9.475\right) \\ \sigma(m,\phi) = \min\left(1.28 \cdot D(m,\phi) + 1.17, 3.09\right) \end{cases} \tag{19}$$

with $D(m,\phi)$ the ice particle size in cm. Note that fragments are considered to have the same rime fraction as the parent particle

Figure 3: Number of ice fragment generated by BRK process at -15°C depending on collision

kinetic energy (CKE) (a) for a 2 mm diameter graupel ($\phi > 0.5$) and (b) for an ice crystal of 4 mm ($\phi < 0.5$).

3.3.2. Ice-ice sticking efficiency

Although the BRK process is commonly addressed when investigating secondary ice processes, the impact of the sticking efficiency (E_s) of ice crystals is frequently overlooked while its effect could be important on this SIP mechanism. Indeed, as shown in Eq. 14 the efficiency of this SIP process varies according to the E_s parameter. Furthermore, the number of ice fragments depend of the size of ice crystals which is linked to the efficiency of aggregation process. In our DESCAM simulations, the sticking efficiency is calculated using two distinct representations.

We use the results of Connolly et al. (2012) (hereafter C12) for temperatures lower than $-5^{\circ}C$ which exhibit a maximum efficiency of 0.6 due to the effect of interlocking dendritic branches that grow at $-15^{\circ}C$. According to Karrer et al. (2021), the sticking efficiency is increasing with the temperature from $-5^{\circ}C$ to reach $E_s = 1$ at $0^{\circ}C$ due to sintering effect (a larger quasi liquid layer in the ice surface which facilitates the sticking of ice crystals). This increase of sticking efficiency has been observed by Hosler and Hallgren (1960) and is also visible considering the maximum dimension of aggregates next $0^{\circ}C$ in (see Lamb and Verlinde, 2011, Fig. 9.22). Furthermore the fill-in effect of ice crystal branches by droplet during riming can reduce the sticking efficiency by inhibiting the interlocking chances of ice asperities, especially next to $-15^{\circ}C$ for the dendritic crystals. We therefore set the sticking efficiency $E_s^{rimed} = 0.15$ at $-15^{\circ}C$ (which corresponds to a mean value found in between -20 and $-10^{\circ}C$). In this first approach, the sticking efficiency depends on rime fraction and is expressed by

$$E_{s,C12}(T,\phi) = (1-\phi)E_{s,C12}^{unrimed} + \phi E_{s,C12}^{rimed}$$

For the second representation, we use the parameterization of Phillips et al. (2015) (hereafter P15) which provides the sticking efficiencies for graupel-ice collisions ($E_{s,P15}^{graupel}$) and ice-ice collisions ($E_{s,P15}^{ice}$) based on laboratory studies. The main difference with $E_{s,C12}$ is that additional parameters are taken into account as the surface area of the colliding particle, temperature, CKE, relative humidity and number of monomers per ice particle. Another difference with the previous representation is that the sticking efficiency is not increasing next to $0^{\circ}\mathrm{C}$, hence, the effect of sintering is not considered. As for $E_{s,C12}$, we represent the transition between graupel-ice and ice-ice sticking efficiency provided by P15 with: $E_{s,P15}(T,\phi) = (1-\phi)E_{s,P15}^{ice} + \phi E_{s,P15}^{graupel}$. Altough this parameterization is based on collision physics, it is difficult to constrain because there are few studies on sticking efficiency. This suggests possible improvements from future studies quantifying sticking efficiency.

All the parameterizations described in Section 3 will be tested in DESCAM model to evaluate the impact of the representation of each of the SIP processes and sticking efficiencies on cloud microphysical properties (Section 5). Simulation setup as well as the observations used to be compared with the simulations will be presented in Section 4.

Name	Hallett-Mossop	HM fragment size	Drop shattering	Ice-ice breakup	Ice-ice breakup fragment size	Sticking efficiency
noSIP	-	-	-	-	-	$E_{s,C12}$
HM1-250	1 per 250 drop	Distributed (see Eq. 3)	-	-	-	$E_{s,C12}$

HM200	200 per mg	Distributed (see Eq. 3)	-	-	-	$E_{s,C12}$
HM350	350 per mg	Distributed (see Eq. 3)	-	-	-	$E_{s,C12}$
HM350-1stbin	350 per mg	2.06 μm (1st bin)	-	-	-	$E_{s,C12}$
HM700	700 per mg	Distributed (see Eq. 3)	-	-	-	$E_{s,C12}$
DS $_{max}$ L21	-	-	Maximum from L21 and K20	-	-	$E_{s,C12}$
DS_P18	-	-	P18	-	-	$E_{s,C12}$
DS_S18	-	-	S18	-	-	$E_{s,C12}$
DS_L15	-	-	L15	-	-	$E_{s,C12}$
BRK_P17	-	-	-	P17	P17	$E_{s,C12}$
BRK_G23	-	-	-	G23	G23	$E_{s,C12}$
BRK_G23_1bin	-	-	-	G23	P17	$E_{s,C12}$
BRK_G23 $_{stick}$ P15	-	-	-	G23	G23	$E_{s,P15}$
ALLSIP	350 per mg	Distributed (see Eq. 3)	P18	G23	G23	$E_{s,C12}$

ALLSIP $_{stick}$ P15	350 per mg	Distributed (see Eq. 3)	P18	G23	G23	$E_{s,P15}$

Table 1: Table of sensitivity tests with different SIP parameterizations. noSIP simulation consider no secondary ice production (only homogeneous and heterogeneous ice nucleation); HM, DS and BRK are simulations considering a single secondary ice production process and respectively investigate the individual parameterization for Hallett-Mossop, Drop shattering and ice-ice breakup. ALLSIP simulations consider the combination of the 3 secondary production mechanisms.

4. Simulation of a deep convective cloud observed during HAIC/HIWC

4.1. HAIC/HIWC observations

An international flight campaign was conducted during two weeks in May 2015 from Cayenne airport (French Guyana) as part of the collaboration between the High Altitude Ice Crystals and High Ice Water Content projects (HAIC/HIWC) (see Fontaine et al., 2020; Hu et al., 2021). During the HAIC/HIWC campaign, in situ cloud measurements were taken using microphysics probes, such as the 2D stereo probe (2D-S), precipitation imaging probe (PIP) and isokinetic probe (IKP2) deployed on the French Falcon 20 aircraft (see Fontaine et al., 2020). Several flight legs (i.e., periods when the aircraft flew at constant altitude) were conducted, enabling the characterization of mean and spread microphysics properties across the altitude of sampled cloud systems .Measurements from the 2D-S and PIP probes provide composite particle size distributions for ice crystals, ranging from 10 μm to 6400 μm. These distributions are used to

derive the number concentration of ice crystals (N_{ice}).

However, as the sampling volume of the 2D-S probe depends on the particle size, even a very small number of particle artifact (e.g. electronic noise or diffraction) can generate an amplified number concentration of ice crystals (Bansemer, 2018). We therefore exclude the ice crystals smaller than 50 μm diameter from both the measurements and simulation results when comparing N_{ice}.

4.2. Model setup

The simulations are performed using a single domain with a grid comprising 354 points in x (Δx = 0.25 km), 210 points in y (Δy = 0.25 km), and 86 points in z (Δz = 0.20 km). The simulation runs for 3 hours with a time step of Δt = 1 s. The atmospheric conditions are derived from a sounding (Fig 4a) observed during the HAIC/HIWC campaign in Cayenne on May 23, 2015. This sounding is representative of the typical conditions encountered during the campaign, characterized by high relative humidity and water vapor mixing ratios at lower altitudes easterly airflow. Note that the wind speed is reduced by a factor of 1.3 below 10 km and by a factor of 2 above, in order to ensure that all the cloud remains within the simulation domain. Furthermore, as this sounding matches a day when in situ measurements were taken at altitudes of 7 km and 11.7 km, it is especially appropriate for comparing PDSs from our simulation with aircraft observations at these levels.

Figure 4: (a) Sounding derived from observations during HAIC/HIWC campaign at Cayenne on the 23th of May 2015 and (b) vertical profile of aerosol particle concentration derived from Ladino et al. (2017).

The simulation is initiated by a thermal perturbation defined as an horizontally circular bubble of 8 km radius (r). Its intensity decreases horizontally depending on radius following a $\cos(r)$ function and exponentially with the altitude. Both maximum latent and sensible fluxes are set to 1500 W m^{-2} which is in the same range of previous studies, such as Lasher-Trapp et al. (2018). The perturbation intensity remains constant for the first 25 minutes before gradually decreasing. The parameters of the bubble (see details in Appendix A) are set to generate a deep convective cloud system with a similar altitude and intensity to those observed in HAIC/HIWC. A similar setup for is used in Huang et al. (2022) to simulate a cloud representative of the HAIC/HIWC campaign.

The concentration of aerosol particles, depicted in Fig. 4b, is derived from measurements of Ladino et al. (2017) carried out during the HAIC/HIWC campaign in Cayenne. Note that the aerosol spectra was extrapolated to smaller sizes as measurements were only taken for aerosol particles with diameters ranging from 0.05 μm to 1 μm. DESCAM represents a type aerosol particle, that presumed to be composed of NaCl (marine origin).

4.3. Cloud development and comparison with observations: no SIP case

Fig. 5 shows the development of the simulated cloud considering no SIP mechanism. After 25 min of simulation, the cloud starts to ascend and reaches its top at 14 km around 50-60 min, forming after that time a distinctive anvil. At this stage the total water content (TWC) is often higher than 2 g m^{-3}. The cloud mature phase occurs between 70 and 110 minutes (Fig. 5 b), about an hour post-formation. During this stage, the anvil becomes prominently visible at the top and the cloud expanded to cover an area of around 100 km^{2}. After 110 minutes, convection starts to

weaken, resulting in a decrease in TWC, and causing the separation of the anvil from the dissipating lower section (Fig. 5 c).

Figure 5: Vertical cross section of total water content of the simulated cloud (noSIP simulation, see Table 1) at different stages (a) at 50 min: formation (b) at 100 min: mature stage and (c) at 150 min: dissipation. Area where TWC $>$ 0.01 g m^{-3} are plotted.

To confront the simulations to the observations, we select specific portions of the simulated cloud that correspond to observed conditions. Indeed, our comparison is limited to values of vertical wind (w) and total water content (TWC) which are in the 5th and 95th percentile of the entire dataset collected on all flight legs of HAIC/HIWC campaign. Thus, the range of vertical wind speed (measured with Rosemount 858 5-hole pressure probe) restricts to [-2.1, 2.5] m s^{-1} and the TWC (measured with the IKP-2 probe) to [0.01, 2.10] g m^{-3}. These limits are used to exclude portions of the simulated cloud which are not sampled and therefore are not representative of observations. Furthermore, this study focuses on the cloud properties at 100 min (in simulation time) given that cloud systems were essentially sampled during their mature phase, as indicated by Fontaine et al. (2020).

Fig. 6 shows the comparison of observed and simulated mean N_{ice} for the simulation including no SIP mechanism as well as for other numerical experiments. Error bars corresponds to the statistical uncertainty of the measurements (with 95% confidence interval) for each leg of the campaign and quantifies the variability of N_{ice} measurements.

In all panels of Fig. 6, the mean N_{ice} is underestimated for the noSIP simulation from 0 to -30°C in comparison to HAIC/HIWC measurements. This discrepancy rises up to 2 orders of

magnitude next to -10°C, as shown in Ladino et al. (2017) where the observed N_{ice} is confronted to the available INP concentration. However, at temperatures lower than -30°C, homogeneous ice nucleation and heterogeneous ice nucleation become strong, resulting in a mean ice concentration greater than 200 L^{-1} which is closer to the range observed during the HAIC/HIWC campaign.

To analyse the properties of ice crystals in more details, Fig. 8a and b shows the observed Particle Size Distributions (PSDs) from HAIC/HIWC campaign (flight #19 on May 23, 2015) at 7.0 and 11.7 km, compared to those from the noSIP simulation at the same altitudes. At 7.0 km (Fig. 8a), the number of small ice crystals (< 1000 μm) is the reason for the observed discrepancies in mean N_{ice}, similarly to previous results obtained with DESCAM model (Kagkara et al., 2020) or with WRF for HAIC/HIWC campaign (Huang et al., 2021). Conversely, at 11.7 km, the simulated PSD (Fig. 8b) gives a higher number of ice crystals close to 90 μm and a lower number of ice crystals between 100-1000 μm compared to observations.

To study the reason of the gap in small ice crystals concentration between observations and the noSIP simulation, numerical experiments are performed for the 3 SIP mechanisms listed in Table 1. Furthermore, several tests for each mechanism are carried out to quantify the effect of different microphysical representations (detailed in Section 3) on ice crystal number concentration (N_{ice}), ice water content (IWC) and PSDs. Finally, the combination of the 3 SIP mechanisms will be studied.

Figure 6: Simulated mean ice crystal (> 50 μm) concentration profiles for different parameterizations of SIP mechanisms, averaged considering the conditions observed during HAIC/HIWC campaign. (a) Simulation with Hallett-Mossop process alone (b) Drop shattering alone (c) ice-ice breakup alone and (d) Combination of all SIP mechanisms. The mean measured

N_{ice} (> 50 μm) from legs of HAIC/HIWC campaign is plotted with an error bar representing the statistical uncertainty of the measurements. The legend indicates the different numerical experiments described in Table. 1. Note that primary ice production processes are always considered.

Figure 7: Mean profiles of simulated IWC (solid lines) and LWC (dashed lines). (a) Simulation with Hallett-Mossop process only (b) Drop shattering only (c) ice-ice breakup only and (d) Combination of all SIP mechanisms. Legend indicates the different numerical experiments described in Table. 1. Note that primary ice production processes are always considered.

5. Results considering individual SIP process

5.1. Impact of the representation of the Hallett-Mossop process

Results of simulations with Hallett-Mossop process alone for N_{ice} are plotted in Fig. 6a for different parameterizations (as detailed in Table. 1). Considering this process allows to increase significantly the mean N_{ice} from 0 to -20°C (similarly to results of Connolly et al., 2006) with up to N_{ice} = 60 L^{-1} at -8°C for HM700. The increase of N_{ice} outside of the HM active range of particle production (see Fig. 1) can be due to the vertical transport of small ice crystals. However, the impact of vertical transport is often ignored for SIP, which can lead to minimize the effect of HM beyond the temperature range of -3 to -8°C. Furthermore, above 8 km, it appears that the presence of HM process leads to a lower N_{ice} than for the noSIP case. This could be explained by the water vapor depletion which inhibits nucleation processes.

Increasing the fragment production rate at -5°C from 200 to 350 fragments per mg results

to increase by two times the mean N_{ice}, whereas increasing HM from 350 to 700 mg^{-1} leads to increase N_{ice} by four (see HM200, HM350 and HM700 in Fig. 6a).

Supposing one fragment per 250 drops (see HM1/250 in Fig. 6a) gives the lowest N_{ice} with a concentration of 10 L^{-1} at -8°C which is 5 times lower than HM350. Indeed as shown in Fig. 1, this can be explained by the fact that a similar mass of rime may consist of a small number of large drops.

Including fragments from HM in the first bin (HM350_1stbin) does not impact N_{ice} or the PSD (not presented here) when compared to simulation HM350 considering distributed fragments having larger sizes.

Mean vertical profiles of ice water content (IWC) and liquid water content (LWC) for each simulation of Table. 1 are presented in Fig. 7. Considering HM (Fig. 7a) results in a rise in IWC by about 0.1 g m^{-3} between 5 and 8 km compared to the noSIP simulation. Conversely, the content of supercooled water between 5 and 8 km decreases by a factor 2 due to HM. This rise in IWC and decrease in supercooled LWC seem proportionally to the number of fragments of each parameterization and coincides to the regions where HM affects the mean N_{ice} in Fig. 6a. Indeed, more numerous ice crystals will increase ice depositional growth from water vapor and drop evaporation (Bergeron-Findeisen effect), as well as riming with more frequent drop-crystal collisions (see Fig. 8 of Part II of this study Grzegorczyk et al., 2024).

However, Fig. 6a also shows that the rime-splintering HM process alone cannot completely explain the observed N_{ice}. Even for the simulation with HM700, which is based on the maximum rate found by Hallett and Mossop (1974), the model results remain one order of magnitude below the observed N_{ice} at -15°C. Indeed, when analyzing the impact of HM on PSDs

at 7.0 km (not shown here), the number of small ice crystals below 1000 μm diameter on PSDs rises but is still lower than the observed concentration especially for 200 μm diameter ice crystals.

Several other studies highlighted that the production rate of ice crystals by the HM process, as it mentioned in Hallett and Mossop (1974), is too low to explain the observed N_{ice} (e.g. Farrington et al., 2016; Young et al., 2019). Furthermore, in some studies, this process is found to be ineffective in augmenting N_{ice} (e.g. Qu et al., 2020; Sotiropoulou et al., 2021b; Zhao et al., 2021). Despite a significant number of laboratory studies, much remains unknown about the physical phenomenon explaining the origin of fragments between -3 to -8°C (Seidel et al., 2024). From our modeling study it remains difficult to conclude whether it is physically more realistic to consider a number or a mass of freezing drops to represent this process, and which rate is the most realistic. However, the HM350 parameterization remains the most used for models and will be applied in this study (in Section 6) when combining several SIP mechanisms.

5.2. Impact of the representation of the Drop shattering process

Considering S18 parameterization for DS leads to no significant effect on the mean N_{ice} (Fig. 6b) or IWC (Fig. 7b) profiles at the mature stage of the cloud. Using P18 also leads to no significant increase for N_{ice} but gives a clear increase in mean IWC from 5 to 8 km. Applying L15 gives a clear rise in N_{ice} from 0 to -10°C but no significant changes in IWC. Finally, using L21 increases strongly N_{ice} up to 20 L^{-1} at 8 km (see DS_{max} L21 in Fig. 6b) as well as IWC (up to 0.5 g m^{-3} at -10°C) which is visible up to 11.5 km. The increase in IWC and the decrease in LWC due to DS are similar to those described for HM.

As presented in Fig. 2b, DS parameterizations are most efficient next to -15°C (except

L15). However, at this level, the number of large droplets significantly decreases compared to lower levels, which is indicated by the quantity of supercooled liquid water which decreases under 0.05 g m^{-3} at -15°C (see the dashed lines in Fig. 7b). Consequently, this mitigates the effect of DS at this level. The largest quantity of supercooled LWC is located close to 0°C in Fig. 7b and is 4 times larger than at -15°C. As the parameterizations of L21 and L15 predicts a large number of ice fragments close to the melting layer, it leads to a large increase of N_{ice} close to this level contrary to other parameterizations. The number of ice crystals generated by DS close to 0°C seems to be particularly important but remain little studied up to now. However, although that using L21 gives a significant increases in mean N_{ice}, the range of observations it still underestimated.

As reported in Fontaine et al. (2020), only a limited number of supercooled water cases were identified during the HAIC/HIWC campaign which is consistent with the low supercooled LWC in our modeling results for the mature stage of the cloud given in Fig. 7. Moreover, as mentioned in Section 4.1, only areas of the simulated cloud corresponding to the observational range (5 to 95 percentile) for TWC and vertical wind speed were used for our comparison. Consequently, regions of strong updrafts ($w > 2$ m s^{-1}) where the supercooled LWC is high are excluded which might even more mitigates the impact of DS in our results.

Our results are similar to the study of Qu et al. (2020) which showed that DS is not significant to produce ice crystals at the mature stage of a similar convective cloud. However, the impact of drop shattering in modeling studies varies. For instance, Qu et al. (2022) found that DS (by using L15) is the most important SIP process and can explain observed concentration at mature stage of a convective system. In contrast, when simulating the same cloud system with the same model (WRF-P3 scheme Morrison and Milbrandt, 2015, for HAIC/HIWC campaign), Huang et al.

(2022) (using P18) found that ice-ice breakup was the most important mechanism at this stage. This indicates that estimating the efficiency of this process remains challenging with the current parameterizations.

Figure 8: Mean particle size distribution of ice crystal at 7.0 km (left column) and 11 km (right column) height, for different representations of ice-ice breakup (BRK) and sticking efficiency. The dashed lines represent the HAIC/HIWC measurements (flight 19) at these altitudes. The area represents the statistical uncertainty of the measurements.

5.3. Impact of the representation of the ice-ice breakup process

For all simulations with ice-ice breakup (Fig. 6c and Fig. 7c), N_{ice} increases by several orders of magnitude between $0^{\circ}C$ and $-30^{\circ}C$ conjointly to the largest rise in IWC which can be up to twice the amount of the noSIP case. Indeed, at 7.0 km the PSDs from simulations including ice-ice breakup (Fig. 8, left column) show a significantly higher number of ice crystals in the 50-1000 μm size range, resulting in a PSD that more closely matches the HAIC/HIWC observations. Additionally, ice-ice breakup leads to the strongest decrease in supercooled LWC in comparison to DS or HM.

In Fig. 6, BRK_P17 simulation gives up to N_{ice} = 20 L^{-1} for $T > -30^{\circ}C$ while BRK_G23 leads up to N_{ice} = 100 L^{-1} which is closer to HAIC/HIWC measurements. Indeed, BRK_P17 simulation in Fig. 8 clearly gives less ice crystals close to 200 μm compared to observations and BRK_G23. This difference was expected regarding Fig. 3 given the fact that the rime fraction of ice crystals is less than 20% above 7.0 km at the mature stage of the cloud (rime content is not illustrated in this study). However, an underestimation of the mean N_{ice} is still

noticeable close to -10°C also when using G23 parameterization with around N_{ice} = 30 L^{-1} compared to the observed mean value of approximately N_{ice} = 100 L^{-1}.

The mean N_{ice} and IWC profiles seem to be relatively insensitive to the change in fragment size as visible when comparing BRK_G23_1bin with BRK_G23 in Fig. 6c. However, when comparing PSDs between Fig 8g and Fig. 8e, it is clear that using distributed fragments (BRK_G23) leads to a maximum at 150 μm which is closer to the mode of the observed PSD. In contrast to that, BRK_G23_1bin gives a higher concentration of ice crystals around 50 μm.

All simulations using C12 sticking efficiency show a strong decrease in IWC with the altitude while N_{ice} increases (e.g. BRK_G23 in Fig. 6c and Fig. 7c). However, when using P15 sticking efficiency, these two profiles become different. First, the curve of BRK_G23 $_{stick}$ P15 shows a higher N_{ice} for T > -10°C compared to BRK_G23 curve. This difference can be attributed to the sintering effect (Karrer et al., 2021) considered in BRK_G23 simulation, causing ice crystals to stick and decrease in number near 0°C. Secondly, both N_{ice} and IWC mean profiles exhibit a minimum next to 8 km for BRK_G23 $_{stick}$ P15. Such decrease in IWC and N_{ice} could be due to the high sticking efficiency next to -15°C (effect of interlocking branches of ice crystals) of P15 parameterization which reduces the ice crystals number. Note that BRK_G23 $_{stick}$ P15 shows a higher N_{ice} in the cloud anvil between -30°C and -50°C compared to BRK_G23.

When comparing Fig. 8e,f with Fig. 8i,j it is also clear that the choice of the sticking efficiency plays a major role on the PSDs shape. Indeed, despite improved N_{ice} considering ice-ice breakup, employing C12 sticking efficiency (Fig. 8e,f) results in an excessive number of ice crystals > 1000 μm at 7.0 km. In contrast, using P15 parameterization (Fig. 8i) yields to a lower number of large ice crystals (> 1000 μm) as well as a mode at 200 μm which is more

consistent with the 250 μm observed PSD mode. However at 11.7 km, using P15 (Fig. 8j) gives an underestimated number of ice crystals of 300-1000 μm compared to simulations using C12 sticking efficiency (Fig. 8f). This highlights that the representation of sticking efficiency significantly impacts the particle size distribution and N_{ice} at both 7.0 and 11.7 km. The fact that ice-ice aggregation strongly impacts the cloud properties was also reported by Qu et al. (2022), underlying the important role of the sticking efficiency on N_{ice} and IWC.

Numerous studies point out ice-ice breakup as a pivotal process to approach observed N_{ice}, IWC or even supercooled LWC, for orographic mixed phase clouds (Dedekind et al., 2021; Georgakaki et al., 2022), convective clouds (Qu et al., 2020; Huang et al., 2022; Patade et al., 2022; Waman et al., 2022; Han et al., 2024) or arctic clouds (Sotiropoulou et al., 2020, 2021b; Zhao et al., 2021; Karalis et al., 2022). Indeed this process can be effective in both mixed phase and ice phase of the cloud which makes it effective at longer time scales contrary to drop shattering or Hallett-Mossop processes which depend on the presence of supercooled liquid drops.

6. Combining all SIP processes

Considering all secondary ice processes together (i.e. combining Hallett-Mossop with HM350, Drop shattering with P18 and ice-ice breakup with G23) results in the combined effects of HM and ice-ice breakup (see Fig. 6d) and thus demonstrate that DS remains weak. The ALLSIP simulation results in a mean N_{ice} profile which is close to that of ice-ice breakup alone (Fig. 6c), with an enhanced N_{ice} near -8°C due to HM process. Indeed, at 6 km, BRK_G23 gives N_{ice} = 20 L^{-1}, HM350 N_{ice} = 30 L^{-1} and ALLSIP gives N_{ice} = 40 L^{-1}. Contrary to Sotiropoulou et al. (2021b) no feedback between ice-ice breakup and HM that could potentially enhance ice

multiplication was observed. The prevailing impact of these two processes are in agreement with the results of Waman et al. (2022).

ALLSIP simulations in Fig. 7d result in similar IWC and supercooled LWC compared to ice-ice breakup alone. The total water content (TWC) given when adding LWC and IWC profile from Fig. 7d (not showed here) is consistent with the observed TWC profiles presented in Fontaine et al. (2020).

Fig. 9a and b show the PSD of ice crystals at 7.0 and 11.7 km for ALLSIP and ALLSIP $_{stick}$ P15. At 7 km, both simulations significantly improve the agreement with the observed PSDs of HAIC/HIWC in comparison to noSIP PSDs (Fig. 8a,b), similarly as for ice-ice breakup alone. Furthermore, P15 gives a better results for PSDs at 7.0 km while at 11.7 km, employing C12 sticking efficiency leads to lower concentrations of ice crystals next to 90 μm diameter which better agree with the measurements. The comparison of ALLSIP and ALLSIP $_{stick}$ P15 (see Fig. 7d, Fig. 6d and Fig. 9a,b) illustrates again the great importance of the representation of sticking efficiency on N_{ice}, IWC and PSDs.

Figure 9: Observed and simulated particle size distributions of ice crystals (a) at 7.0 km and (b) at 11.7 km. Simulations combining all SIP mechanisms using C12 sticking efficiency, (labeled ALLSIP) or C12 sticking efficiency, (labeled ALLSIP $_{stick}$ P15)

7. Conclusions

This paper investigates the representation of Hallett-Mossop (HM), Drop shattering (DS) Ice-ice breakup (BRK) processes by simulating an idealized convective cloud representing a cloud that was observed during the HAIC/HIWC campaign with the bin microphysics scheme

DESCAM. The properties of the simulated cloud (at its mature stage) are compared to in situ cloud measurements conducted during the campaign.

At the cloud mature stage our results show that the BRK and HM are key processes that can explain the observed ice concentration of the HAIC/HIWC when $T > -30^{\circ}\mathrm{C}$. The strong impact of BRK has been observed in numerous studies (Qu et al., 2020; Huang et al., 2022; Waman et al., 2023) for convective clouds. Despite that, its exact quantification remains uncertain due to only 4 dedicated laboratory studies. We found better coherence between simulated and observed N_{ice}, as well as ice crystal particle size distributions when using coefficients from Grzegorczyk et al. (2023) for BRK compared to the original one from Phillips et al. (2017).

Our results show that HM impacts a broader temperature range (0 to $-20^{\circ}\mathrm{C}$) than its active production range (-3 to $-8^{\circ}\mathrm{C}$) and impacts N_{ice} in the same magnitude as BRK for $T < -15^{\circ}\mathrm{C}$. Although the HM process has been studied a lot in the past and very often included in microphysics scheme, its physical origin is not well understood yet. However, representing this process with different rates, depending on rime mass or number of rimed drops impact strongly the results. Recently, the laboratory study of Seidel et al. (2024) depicts only a negligible rate of fragment production compared to previous studies which could question the importance and highlight the uncertain origin of HM process.

We found that the effect of DS process on the mean N_{ice} is weak at the cloud mature stage, which is in contrast with the results of Qu et al. (2022) for the same observational case. However, this process could be important in the cloud development stage (see Lawson et al., 2017, 2023) as well as in other clouds types where large drops are present. Although this process appears to be better understood than HM and better characterized than BRK, it is still poorly studied for temperatures close to $0^{\circ}\mathrm{C}$, despite the presence of the largest quantity of supercooled water at this

level. Furthermore, as demontrated by Keinert et al. (2020), DS depends on numerous parameters that remain not well quantified yet.

In the literature, modeling studies including both HM and DS processes for the production of ice crystals often give different contributions of these two processes, as in Qu et al. (2020) where DS is stronger than HM while Waman et al. (2023) found the inverse results. This difference may be due to the representation of warm microphysical processes which do not follow the same microphysical description. Indeed, the sparse representation of collision-coalescence and drop breakup processes for liquid drops (as shown by Tridon et al., 2019; Planche et al., 2019; Morrison et al., 2020; Niquet et al., 2024) in models can affect droplet size distribution which may play a role for both HM and DS processes and therefore the ice phase of clouds.

Our results also highlight that the representation of sticking efficiency affects significantly the profiles of N_{ice} as well as the shape of PSDs across different levels of the cloud.

We demonstrate the importance of SIP processes and sticking efficiency which depend on ice-ice and drop-ice collisions. Quantitative information about these interactions are still lacking which lead to uncertain representation of several ice microphysical processes in models. Extending experimental laboratory studies (e.g. Keinert et al., 2020; James et al., 2021; Grzegorczyk et al., 2023; Seidel et al., 2024) could bring crucial information to fill this gap.

Our results presented in this paper restrict to the analysis of the vertical structure of IWC, LWC, N_{ice} as well as ice crystals size distribution. The different SIP processes also influence significantly the cloud dynamics, vertical wind speed, the vertical extension of the cloud, water vapor field and rainfall. Part II of this study (Grzegorczyk et al., 2024) will focus on the temporal evolution of ice production through SIP and PIP processes, assess the contribution of each mechanism at different stages of cloud development and examine their effect on the evolution of

particle size distributions. Additionally, the impacts of SIP on relative humidity, rainfall, and cloud dynamics, including vertical wind speed and cloud top will be addressed to quantify the effect and importance of these processes for cloud microphysics.

Appendix A. Cloud initiation

The sensible and latent fluxes to initiate the convection are spatially and temporally described by

$$F = F_{max} \cdot f(x,y) \cdot f(t) \cdot \exp(-z/\alpha) \tag{A.1}$$

with F_{max} = 1500 W m $^{-2}$ the maximum flux, the time dependency $f(t)$, the horizontal dependency $f(x,y)$ and the attenuation length is α = 0.95 km. The horizontal dependency of the perturbation $f(x,y)$ is expressed by

$$f(x,y) = \begin{cases} \cos\left(\frac{\pi}{2 \times R_b}\sqrt{(x_0-x)^2+(y_0-y)^2}\right) \text{for} \sqrt{(x_0-x)^2+(y_0-y)^2} \le R_b \\ 0 \text{ for} \sqrt{(x_0-x)^2+(y_0-y)^2} > R_b \end{cases} \tag{A.2}$$

with x_0 = 55 km and y_0 = 35 km the coordinates of center of the perturbation, R_b = 8 km is the radius of the perturbation. The time dependency $f(t)$ is expressed by

$$f(t) = \begin{cases} \left(\frac{1500}{t}\right)^{1.5} \text{ for } t \ge 1500 \\ 1 \text{ for } t < 1500 \end{cases} \tag{A.3}$$

with t the time of the simulation in s. A similar size of perturbation is used in Huang et al. (2022) with 10 km radius to study the convective clouds of the HAIC/HIWC campaign.

Acknowledgements

This work is part of project ACME funded by the Agence Nationale de la Recherche (ANR) under the JCJC program, reference ANR-21-CE01-0003. The contribution from the lead author has been founded by the ACME project. This work was granted access to the HPC resources of [CINES/IDRIS/TGCC] under the allocations A0100105056 and A0160115061 made by GENCI. We thank the team from HAIC/HIWC program for their contribution to data collection and sharing on the AERIS database. We acknowledge Alexei Korolev, Luis Ladino, Climate Change Canada (ECCC) and National Research Council (NRC) for sharing the UHSAS datasets.

References

Arteaga, D., Planche, C., Kagkara, C., Wobrock, W., Banson, S., Tridon, F., Flossmann, A., 2020. Evaluation of two cloud-resolving models using bin or bulk microphysics representation for the hymex-iop7a heavy precipitation event. Atmosphere 11, 1177. URL: http://dx.doi.org/10.3390/atmos11111177, doi: 10.3390/atmos11111177.

Bansemer, A., 2018. A multi-instrument comparison of small ice particle size distributions measured from aircraft, in: AMS 15th Conference on Cloud Physics.

Beard, K.V., Ochs, H.T., 1995. Collisions between small precipitation drops. part ii: Formulas for coalescence, temporary coalescence, and satellites. Journal of the Atmospheric Sciences 52, 3977–3996. URL: http://dx.doi.org/10.1175/1520-0469(1995)052<3977:CBSPDP>2.0.CO;2, doi: 10.1175/1520-0469(1995)052<3977:cbspdp>2.0.co;2.

Böhm, J.P., 1992a. A general hydrodynamic theory for mixed-phase microphysics. part i: Drag and fall speed of hydrometeors. Atmospheric research 27, 253–274.

Böhm, J.P., 1992b. A general hydrodynamic theory for mixed-phase microphysics. part ii:

Collision kernels for coalescence. Atmospheric research 27, 275–290.

Böhm, J.P., 1992c. A general hydrodynamic theory for mixed-phase microphysics. part iii: Riming and aggregation. Atmospheric research 28, 103–123.

Bott, A., 1998. A flux method for the numerical solution of the stochastic collection equation. Journal of the Atmospheric Sciences 55, 2284–2293. URL: https://doi.org/10.1175/1520-0469(1998)055<2284:afmftn>2.0.co;2, doi: 10.1175/1520-0469(1998)055<2284:afmftn>2.0.co;2.

Brechner, P., McFarquhar, G.M., Schwarzenboeck, A., Korolev, A.V., 2023. Ice crystal size distributions in tropical mesoscale convective systems in the vicinity of darwin, australia: Results from the HAIC/HIWC campaign. Journal of the Atmospheric Sciences 80, 2147–2164. URL: https://doi.org/10.1175/jas-d-22-0209.1, doi: 10.1175/jas-d-22-0209.1.

Choularton, T., Latham, J., Mason, B.J., 1978. A possible mechanism of ice splinter production during riming. Nature 274, 791–792.

Choularton, T.W., Griggs, D.J., Humood, B.Y., Latham, J., 1980. Laboratory studies of riming, and its relation to ice splinter production. Quarterly Journal of the Royal Meteorological Society 106, 367–374. URL: https://doi.org/10.1002/qj.49710644809, doi: 10.1002/qj.49710644809.

Clark, T., Hall, W., Coen, J., 1996. Source Code Documentation for the Clark-Hall Cloud-scale Model Code Version G3CH01. Technical Report. URL: http://opensky.ucar.edu/islandora/object/technotes:193, doi: 10.5065/D67W694V.

Clark, T.L., 2003. Block-iterative method of solving the nonhydrostatic pressure in

terrain-following coordinates: Two-level pressure and truncation error analysis. Journal of Applied Meteorology 42, 970–983. URL: http://dx.doi.org/10.1175/1520-0450(2003)042<0970:BMOSTN>2.0.CO;2, doi: 10.1175/1520-0450(2003)042<0970:bmostn>2.0.co;2.

Cober, S.G., List, R., 1993. Measurements of the heat and mass transfer parameters characterizing conical graupel growth. J. Atmos. Sci. 50, 1591–1609.

Connolly, P., Emersic, C., Field, P., 2012. A laboratory investigation into the aggregation efficiency of small ice crystals. Atmospheric Chemistry and Physics 12, 2055–2076.

Connolly, P.J., Heymsfield, A.J., Choularton, T.W., 2006. Modelling the influence of rimer surface temperature on the glaciation of intense thunderstorms: The rime–splinter mechanism of ice multiplication. Quarterly Journal of the Royal Meteorological Society 132, 3059–3077. URL: http://dx.doi.org/10.1256/qj.05.45, doi: 10.1256/qj.05.45.

Cotton, W.R., Tripoli, G.J., Rauber, R.M., Mulvihill, E.A., 1986. Numerical simulation of the effects of varying ice crystal nucleation rates and aggregation processes on orographic snowfall. Journal of Climate and Applied Meteorology 25, 1658–1680. URL: https://doi.org/10.1175/1520-0450(1986)025<1658:nsoteo>2.0.co;2, doi: 10.1175/1520-0450(1986)025<1658:nsoteo>2.0.co;2.

Dedekind, Z., Lauber, A., Ferrachat, S., Lohmann, U., 2021. Sensitivity of precipitation formation to secondary ice production in winter orographic mixed-phase clouds. Atmospheric Chemistry and Physics 21, 15115–15134. URL: https://acp.copernicus.org/articles/21/15115/2021/, doi: 10.5194/acp-21-15115-2021.

Deshmukh, A., Phillips, V.T., Bansemer, A., Patade, S., Waman, D., 2022. New empirical

formulation for the sublimational breakup of graupel and dendritic snow. Journal of the Atmospheric Sciences 79, 317–336.

Farrington, R.J., Connolly, P.J., Lloyd, G., Bower, K.N., Flynn, M.J., Gallagher, M.W., Field, P.R., Dearden, C., Choularton, T.W., 2016. Comparing model and measured ice crystal concentrations in orographic clouds during the INUPIAQ campaign. Atmospheric Chemistry and Physics 16, 4945–4966. URL: https://doi.org/10.5194/acp-16-4945-2016, doi: 10.5194/acp-16-4945-2016.

Field, P.R., Lawson, R.P., Brown, P.R.A., Lloyd, G., Westbrook, C., Moisseev, D., Miltenberger, A., Nenes, A., Blyth, A., Choularton, T., Connolly, P., Buehl, J., Crosier, J., Cui, Z., Dearden, C., DeMott, P., Flossmann, A., Heymsfield, A., Huang, Y., Kalesse, H., Kanji, Z.A., Korolev, A., Kirchgaessner, A., Lasher-Trapp, S., Leisner, T., McFarquhar, G., Phillips, V., Stith, J., Sullivan, S., 2017. Chapter 7. secondary ice production - current state of the science and recommendations for the future. Meteorological Monographs doi: 10.1175/amsmonographs-d-16-0014.1.

Flossmann, A.I., Wobrock, W., 2010. A review of our understanding of the aerosol–cloud interaction from the perspective of a bin resolved cloud scale modelling. Atmospheric Research 97, 478–497. URL: https://www.sciencedirect.com/science/article/pii/S0169809510001249, doi: https://doi.org/10.1016/j.atmosres.2010.05.008. from the Lab to Models and Global Observations: Hans R. Pruppacher and Cloud Physics.

Fontaine, E., 2014. Masse des cristaux de glace et facteurs de réflectivité radar dans les systèmes de nuages convectifs de moyenne échelle formés dans les Tropiques et la région de la mer

Méditerranée. Theses. Université Blaise Pascal - Clermont-Ferrand II. URL: https://theses.hal.science/tel-01176222.

Fontaine, E., Schwarzenboeck, A., Leroy, D., Delanoë, J., Protat, A., Dezitter, F., Strapp, J.W., Lilie, L.E., 2020. Statistical analysis of ice microphysical properties in tropical mesoscale convective systems derived from cloud radar and in situ microphysical observations. Atmospheric Chemistry and Physics 20, 3503–3553. URL: http://dx.doi.org/10.5194/acp-20-3503-2020, doi: 10.5194/acp-20-3503-2020.

Georgakaki, P., Sotiropoulou, G., Vignon, E., Billault-Roux, A.C., Berne, A., Nenes, A., 2022. Secondary ice production processes in wintertime alpine mixed-phase clouds. Atmospheric Chemistry and Physics 22, 1965–1988. URL: https://acp.copernicus.org/articles/22/1965/2022/, doi: 10.5194/acp-22-1965-2022.

Griggs, D.J., Choularton, T.W., 1986. A laboratory study of secondary ice particle production by the fragmentation of rime and vapour-grown ice crystals. Quarterly Journal of the Royal Meteorological Society 112, 149–163. URL: https://onlinelibrary.wiley.com/doi/10.1002/qj.49711247109, doi: 10.1002/qj.49711247109.

Grzegorczyk, P., Wobrock, W., Canzi, A., Niquet, L., Tridon, F., Planche, C., 2024. Investigating secondary ice production in a deep convective cloud with a 3d bin microphysics model: Part ii - effects on the cloud development. Submitted to Atmospheric Research.

Grzegorczyk, P., Yadav, S., Zanger, F., Theis, A., Mitra, S.K., Borrmann, S., Szakáll, M., 2023. Fragmentation of ice particles: laboratory experiments on graupel–graupel and

graupel–snowflake collisions. Atmospheric Chemistry and Physics 23, 13505–13521. URL: https://acp.copernicus.org/articles/23/13505/2023/, doi: 10.5194/acp-23-13505-2023.

Hallett, J., Mossop, S.C., 1974. Production of secondary ice particles during the riming process. Nature 249, 26–28. URL: https://doi.org/10.1038/249026a0, doi: 10.1038/249026a0.

Hallett, J., Sax, R.I., Lamb, D., Murty, A.S.R., 1978. Aircraft measurements of ice in florida cumuli. Quarterly Journal of the Royal Meteorological Society 104, 631–651. URL: https://doi.org/10.1002/qj.49710444108, doi: 10.1002/qj.49710444108.

Han, C., Hoose, C., Dürlich, V., 2024. Secondary ice production in simulated deep convective clouds: A sensitivity study. Journal of the Atmospheric Sciences 81, 903–921. URL: http://dx.doi.org/10.1175/JAS-D-23-0156.1, doi: 10.1175/jas-d-23-0156.1.

Heymsfield, A., Szakáll, M., Jost, A., Giammanco, I., Wright, R., 2018. A comprehensive observational study of graupel and hail terminal velocity, mass flux, and kinetic energy. Journal of the Atmospheric Sciences 75, 3861–3885. URL: https://doi.org/10.1175/jas-d-18-0035.1, doi: 10.1175/jas-d-18-0035.1.

Heymsfield, A., Willis, P., 2014. Cloud conditions favoring secondary ice particle production in tropical maritime convection. Journal of the Atmospheric Sciences 71, 4500–4526. URL: http://dx.doi.org/10.1175/JAS-D-14-0093.1, doi: 10.1175/jas-d-14-0093.1.

Heymsfield, A.J., Mossop, S.C., 1984. Temperature dependence of secondary ice crystal production during soft hail growth by riming. Quarterly Journal of the Royal Meteorological Society 110, 765–770. URL: http://dx.doi.org/10.1002/qj.49711046512, doi: 10.1002/qj.49711046512.

Heymsfield, A.J., Schmitt, C., Chen, C.C.J., Bansemer, A., Gettelman, A., Field, P.R., Liu, C., 2020. Contributions of the liquid and ice phases to global surface precipitation: Observations and global climate modeling. Journal of the Atmospheric Sciences 77, 2629–2648. URL: http://dx.doi.org/10.1175/jas-d-19-0352.1, doi: 10.1175/jas-d-19-0352.1.

Heymsfield, A.J., Westbrook, C.D., 2010. Advances in the estimation of ice particle fall speeds using laboratory and field measurements. Journal of the Atmospheric Sciences 67, 2469–2482. URL: https://doi.org/10.1175/2010jas3379.1, doi: 10.1175/2010jas3379.1.

Hiron, T., Flossmann, A., 2015. A study of the role of the parameterization of heterogeneous ice nucleation for the modeling of microphysics and precipitation of a convective cloud. Journal of the Atmospheric Sciences 72, 3322–3339.

Hoarau, T., Pinty, J.P., Barthe, C., 2018. A representation of the collisional ice break-up process in the two-moment microphysics lima v1.0 scheme of meso-nh. Geoscientific Model Development 11, 4269–4289. URL: https://gmd.copernicus.org/articles/11/4269/2018/, doi: 10.5194/gmd-11-4269-2018.

Hobbs, P.V., Farber, R., 1972. Types of snowfall. Journal de Recherches Atmosphériques 6, 245–258.

Hobbs, P.V., Politovich, M.K., Radke, L.F., 1980. The structures of summer convective clouds in eastern montana. i: Natural clouds. Journal of Applied Meteorology 19, 645–663. doi: 10.1175/1520-0450(1980)019<0645:tsoscc>2.0.co;2.

Hobbs, P.V., Rangno, A.L., 1985. Ice particle concentrations in clouds. Journal of the atmospheric sciences 42, 2523–2549.

Hosler, C., Hallgren, R., 1960. The aggregation of small ice crystals. Discussions of the Faraday Society 30, 200–207.

Hu, Y., McFarquhar, G.M., Wu, W., Huang, Y., Schwarzenboeck, A., Protat, A., Korolev, A., Rauber, R.M., Wang, H., 2021. Dependence of ice microphysical properties on environmental parameters: Results from haic-hiwc cayenne field campaign. Journal of the Atmospheric Sciences URL: http://dx.doi.org/10.1175/JAS-D-21-0015.1, doi: 10.1175/jas-d-21-0015.1.

Huang, Y., Wu, W., McFarquhar, G.M., Wang, X., Morrison, H., Ryzhkov, A., Hu, Y., Wolde, M., Nguyen, C., Schwarzenboeck, A., Milbrandt, J., Korolev, A.V., Heckman, I., 2021. Microphysical processes producing high ice water contents (hiwcs) in tropical convective clouds during the haic-hiwc field campaign: evaluation of simulations using bulk microphysical schemes. Atmospheric Chemistry and Physics 21, 6919–6944. URL: http://dx.doi.org/10.5194/acp-21-6919-2021, doi: 10.5194/acp-21-6919-2021.

Huang, Y., Wu, W., McFarquhar, G.M., Xue, M., Morrison, H., Milbrandt, J., Korolev, A.V., Hu, Y., Qu, Z., Wolde, M., Nguyen, C., Schwarzenboeck, A., Heckman, I., 2022. Microphysical processes producing high ice water contents (hiwcs) in tropical convective clouds during the haic-hiwc field campaign: dominant role of secondary ice production. Atmospheric Chemistry and Physics 22, 2365–2384. URL: https://acp.copernicus.org/articles/22/2365/2022/, doi: 10.5194/acp-22-2365-2022.

James, R.L., Phillips, V.T.J., Connolly, P.J., 2021. Secondary ice production during the break-up of freezing water drops on impact with ice particles. Atmospheric Chemistry and Physics 21,

18519–18530. URL: https://doi.org/10.5194/acp-21-18519-2021, doi: 10.5194/acp-21-18519-2021.

Jiusto, J.E., Weickmann, H., 1973. Types of snowfall. Bulletin of the American Meteorological Society 54, 1148–1162.

Kagkara, C., Wobrock, W., Planche, C., Flossmann, A.I., 2020. The sensitivity of intense rainfall to aerosol particle loading – a comparison of bin-resolved microphysics modelling with observations of heavy precipitation from hymex iop7a. Natural Hazards and Earth System Sciences 20, 1469–1483. URL: http://dx.doi.org/10.5194/nhess-20-1469-2020, doi: 10.5194/nhess-20-1469-2020.

Kanji, Z.A., Ladino, L.A., Wex, H., Boose, Y., Burkert-Kohn, M., Cziczo, D.J., Krämer, M., 2017. Overview of ice nucleating particles. Meteorological Monographs 58, 1.1–1.33. URL: http://dx.doi.org/10.1175/amsmonographs-d-16-0006.1, doi: 10.1175/amsmonographs-d-16-0006.1.

Karalis, M., Sotiropoulou, G., Abel, S.J., Bossioli, E., Georgakaki, P., Methymaki, G., Nenes, A., Tombrou, M., 2022. Effects of secondary ice processes on a stratocumulus to cumulus transition during a cold-air outbreak. Atmospheric Research 277, 106302. URL: http://dx.doi.org/10.1016/j.atmosres.2022.106302, doi: 10.1016/j.atmosres.2022.106302.

Karrer, M., Seifert, A., Ori, D., Kneifel, S., 2021. Improving the representation of aggregation in a two-moment microphysical scheme with statistics of multi-frequency doppler radar observations. Atmospheric Chemistry and Physics 21, 17133–17166. URL: https://acp.copernicus.org/articles/21/17133/2021/, doi:

10.5194/acp-21-17133-2021.

Keinert, A., Spannagel, D., Leisner, T., Kiselev, A., 2020. Secondary ice production upon freezing of freely falling drizzle droplets. Journal of the Atmospheric Sciences 77, 2959–2967. URL: http://dx.doi.org/10.1175/jas-d-20-0081.1, doi: 10.1175/jas-d-20-0081.1.

Khain, A., Lynn, B., 2009. Simulation of a supercell storm in clean and dirty atmosphere using weather research and forecast model with spectral bin microphysics. Journal of Geophysical Research 114. URL: https://doi.org/10.1029/2009jd011827, doi: 10.1029/2009jd011827.

Koop, T., Luo, B., Tsias, A., Peter, T., 2000. Water activity as the determinant for homogeneous ice nucleation in aqueous solutions. Nature 406, 611–614. URL: http://dx.doi.org/10.1038/35020537, doi: 10.1038/35020537.

Korolev, A., Heckman, I., Wolde, M., Ackerman, A.S., Fridlind, A.M., Ladino, L.A., Lawson, R.P., Milbrandt, J., Williams, E., 2020. A new look at the environmental conditions favorable to secondary ice production. Atmospheric Chemistry and Physics 20, 1391–1429. URL: http://dx.doi.org/10.5194/acp-20-1391-2020, doi: 10.5194/acp-20-1391-2020.

Korolev, A., Leisner, T., 2020. Review of experimental studies of secondary ice production. Atmospheric Chemistry and Physics 20, 11767–11797. doi: 10.5194/acp-20-11767-2020.

Korolev, A., McFarquhar, G., Field, P.R., Franklin, C., Lawson, P., Wang, Z., Williams, E., Abel, S.J., Axisa, D., Borrmann, S., Crosier, J., Fugal, J., Krämer, M., Lohmann, U., Schlenczek, O., Schnaiter, M., Wendisch, M., 2017. Mixed-phase clouds: Progress and challenges. Meteorological Monographs 58, 5.1–5.50. URL: http://dx.doi.org/10.1175/AMSMONOGRAPHS-D-17-0001.1, doi:

10.1175/amsmonographs-d-17-0001.1.

Korolev, A.V., Emery, E.F., Strapp, J.W., Cober, S.G., Isaac, G.A., Wasey, M., Marcotte, D., 2011. Small ice particles in tropospheric clouds: Fact or artifact? airborne icing instrumentation evaluation experiment. Bulletin of the American Meteorological Society 92, 967–973. URL: http://dx.doi.org/10.1175/2010BAMS3141.1, doi: 10.1175/2010bams3141.1.

Lachapelle, M., Thériault, J.M., 2022. Characteristics of precipitation particles and microphysical processes during the 11–12 january 2020 ice pellet storm in the montréal area, québec, canada. Monthly Weather Review 150, 1043–1059. URL: http://dx.doi.org/10.1175/MWR-D-21-0185.1, doi: 10.1175/mwr-d-21-0185.1.

Ladino, L.A., Korolev, A., Heckman, I., Wolde, M., Fridlind, A.M., Ackerman, A.S., 2017. On the role of ice-nucleating aerosol in the formation of ice particles in tropical mesoscale convective systems. Geophysical Research Letters 44, 1574–1582. URL: https://agupubs.onlinelibrary.wiley.com/doi/abs/10.1002/2016GL072455, doi: https://doi.org/10.1002/2016GL072455, arXiv:https://agupubs.onlinelibrary.wiley.com/doi/pdf/10.1002/2016GL072455.

Lamb, D., Verlinde, J., 2011. Physics and Chemistry of Clouds. Cambridge University Press. URL: https://doi.org/10.1017/cbo9780511976377, doi: 10.1017/cbo9780511976377.

Lasher-Trapp, S., Kumar, S., Moser, D.H., Blyth, A.M., French, J.R., Jackson, R.C., Leon, D.C., Plummer, D.M., 2018. On different microphysical pathways to convective rainfall. Journal of

Applied Meteorology and Climatology 57, 2399–2417. URL: https://doi.org/10.1175/jamc-d-18-0041.1, doi: 10.1175/jamc-d-18-0041.1.

Lauber, A., Henneberger, J., Mignani, C., Ramelli, F., Pasquier, J.T., Wieder, J., Hervo, M., Lohmann, U., 2021. Continuous secondary-ice production initiated by updrafts through the melting layer in mountainous regions. Atmospheric Chemistry and Physics 21, 3855–3870. URL: https://doi.org/10.5194/acp-21-3855-2021, doi: 10.5194/acp-21-3855-2021.

Lauber, A., Kiselev, A., Pander, T., Handmann, P., Leisner, T., 2018. Secondary ice formation during freezing of levitated droplets. Journal of the Atmospheric Sciences 75, 2815–2826. URL: http://dx.doi.org/10.1175/jas-d-18-0052.1, doi: 10.1175/jas-d-18-0052.1.

Lawson, P., Gurganus, C., Woods, S., Bruintjes, R., 2017. Aircraft observations of cumulus microphysics ranging from the tropics to midlatitudes: Implications for a "new" secondary ice process. Journal of the Atmospheric Sciences 74, 2899–2920. URL: http://dx.doi.org/10.1175/JAS-D-17-0033.1, doi: 10.1175/jas-d-17-0033.1.

Lawson, R.P., Korolev, A.V., DeMott, P.J., Heymsfield, A.J., Bruintjes, R.T., Wolff, C.A., Woods, S., Patnaude, R.J., Jensen, J.B., Moore, K.A., Heckman, I., Rosky, E., Haggerty, J., Perkins, R.J., Fisher, T., Hill, T.C.J., 2023. The secondary production of ice in cumulus experiment (spicule). Bulletin of the American Meteorological Society 104, E51–E76. URL: http://dx.doi.org/10.1175/BAMS-D-21-0209.1, doi: 10.1175/bams-d-21-0209.1.

Lawson, R.P., Woods, S., Morrison, H., 2015. The microphysics of ice and precipitation development in tropical cumulus clouds. Journal of the Atmospheric Sciences 72, 2429–2445.

URL: https://doi.org/10.1175/jas-d-14-0274.1, doi: 10.1175/jas-d-14-0274.1.

Leisner, T., Pander, T., Handmann, P., Kiselev, A., 2014. Secondary ice processes upon heterogeneous freezing of cloud droplets. URL: https://ams.confex.com/ams/14CLOUD14ATRAD/webprogram/Paper250221.html. 14th Conf. on Cloud Physics and Atmospheric Radiation, Amer. Meteor. Soc, Boston, MA.

Lew, J.K., Kingsmill, D.E., Montague, D.C., 1985. A theoretical study of the collision efficiency of small planar ice crystals colliding with large supercooled water drops. Journal of the Atmospheric Sciences 42, 857–862. URL: https://doi.org/10.1175/1520-0469(1985)042<0857:atsotc>2.0.co;2, doi: 10.1175/1520-0469(1985)042<0857:atsotc>2.0.co;2.

Low, T.B., List, R., 1982. Collision, coalescence and breakup of raindrops. part II: Parameterization of fragment size distributions. Journal of the Atmospheric Sciences 39, 1607–1619. URL: https://doi.org/10.1175/1520-0469(1982)039<1607:ccabor>2.0.co;2, doi: 10.1175/1520-0469(1982)039<1607:ccabor>2.0.co;2.

Mansell, E.R., Ziegler, C.L., 2013. Aerosol effects on simulated storm electrification and precipitation in a two-moment bulk microphysics model. Journal of the Atmospheric Sciences 70, 2032 – 2050. URL: https://journals.ametsoc.org/view/journals/atsc/70/7/jas-d-12-0264.1.xml, doi: 10.1175/JAS-D-12-0264.1.

Matus, A.V., L'Ecuyer, T.S., 2017. The role of cloud phase in earth's radiation budget. Journal of

Geophysical Research: Atmospheres 122, 2559–2578. URL: http://dx.doi.org/10.1002/2016JD025951, doi: 10.1002/2016jd025951.

Monier, M., Wobrock, W., Gayet, J.F., Flossmann, A., 2006. Development of a detailed microphysics cirrus model tracking aerosol particles' histories for interpretation of the recent inca campaign. Journal of the Atmospheric Sciences 63, 504–525. URL: http://dx.doi.org/10.1175/JAS3656.1, doi: 10.1175/jas3656.1.

Morrison, H., Grabowski, W.W., 2010. An improved representation of rimed snow and conversion to graupel in a multicomponent bin microphysics scheme. Journal of the Atmospheric Sciences 67, 1337–1360. URL: https://doi.org/10.1175/2010jas3250.1, doi: 10.1175/2010jas3250.1.

Morrison, H., van Lier-Walqui, M., Fridlind, A.M., Grabowski, W.W., Harrington, J.Y., Hoose, C., Korolev, A., Kumjian, M.R., Milbrandt, J.A., Pawlowska, H., Posselt, D.J., Prat, O.P., Reimel, K.J., Shima, S., van Diedenhoven, B., Xue, L., 2020. Confronting the challenge of modeling cloud and precipitation microphysics. Journal of Advances in Modeling Earth Systems 12. URL: http://dx.doi.org/10.1029/2019MS001689, doi: 10.1029/2019ms001689.

Morrison, H., Milbrandt, J.A., 2015. Parameterization of cloud microphysics based on the prediction of bulk ice particle properties. part i: Scheme description and idealized tests. Journal of the Atmospheric Sciences 72, 287 – 311. URL: https://journals.ametsoc.org/view/journals/atsc/72/1/jas-d-14-0065.1.xml, doi: 10.1175/JAS-D-14-0065.1.

Morrison, H., Thompson, G., Tatarskii, V., 2009. Impact of cloud microphysics on the development of trailing stratiform precipitation in a simulated squall line: Comparison of one-

and two-moment schemes. Monthly Weather Review 137, 991–1007. URL: http://dx.doi.org/10.1175/2008MWR2556.1, doi: 10.1175/2008mwr2556.1.

Mossop, S.C., 1976. Production of secondary ice particles during the growth of graupel by riming. Quarterly Journal of the Royal Meteorological Society 102, 45–57. URL: https://doi.org/10.1002/qj.49710243104, doi: 10.1002/qj.49710243104.

Niquet, L., Tridon, F., Grzegorczyk, P., Causse, A., Bordet, B., Wobrock, W., Planche, C., 2024. Evaluation of the representation of raindrop self-collection and breakup in two-moment bulk models using a multifrequency radar retrieval. Journal of Geophysical Research: Atmospheres 129. URL: http://dx.doi.org/10.1029/2024JD041269, doi: 10.1029/2024jd041269.

Patade, S., Waman, D., Deshmukh, A., Gupta, A.K., Jadav, A., Phillips, V.T.J., Bansemer, A., Carlin, J., Ryzhkov, A., 2022. The influence of multiple groups of biological ice nucleating particles on microphysical properties of mixed-phase clouds observed during mc3e. Atmospheric Chemistry and Physics 22, 12055–12075. URL: https://acp.copernicus.org/articles/22/12055/2022/, doi: 10.5194/acp-22-12055-2022.

Phillips, V.T.J., Formenton, M., Bansemer, A., Kudzotsa, I., Lienert, B., 2015. A Parameterization of Sticking Efficiency for Collisions of Snow and Graupel with Ice Crystals: Theory and Comparison with Observations*. Journal of the Atmospheric Sciences 72, 4885–4902. doi: 10.1175/JAS-D-14-0096.1.

Phillips, V.T.J., Patade, S., Gutierrez, J., Bansemer, A., 2018. Secondary ice production by fragmentation of freezing drops: Formulation and theory. Journal of the Atmospheric Sciences 75, 3031–3070. URL: https://doi.org/10.1175/jas-d-17-0190.1,

doi: 10.1175/jas-d-17-0190.1.

Phillips, V.T.J., Yano, J.I., Khain, A., 2017. Ice Multiplication by Breakup in Ice–Ice Collisions. Part I: Theoretical Formulation. Journal of the Atmospheric Sciences 74, 1705–1719. doi: 10.1175/JAS-D-16-0224.1.

Planche, C., Tridon, F., Banson, S., Thompson, G., Monier, M., Battaglia, A., Wobrock, W., 2019. On the realism of the rain microphysics representation of a squall line in the wrf model. part ii: Sensitivity studies on the rain drop size distributions. Monthly Weather Review 147, 2811–2825. URL: http://dx.doi.org/10.1175/MWR-D-18-0019.1, doi: 10.1175/mwr-d-18-0019.1.

Planche, C., Wobrock, W., Flossmann, A.I., 2014. The continuous melting process in a cloud-scale model using a bin microphysics scheme. Quarterly Journal of the Royal Meteorological Society 140, 1986–1996.

Planche, C., Wobrock, W., Flossmann, A.I., Tridon, F., Van Baelen, J., Pointin, Y., Hagen, M., 2010. The influence of aerosol particle number and hygroscopicity on the evolution of convective cloud systems and their precipitation: A numerical study based on the cops observations on 12 august 2007. Atmospheric Research 98, 40–56. URL: http://dx.doi.org/10.1016/j.atmosres.2010.05.003, doi: 10.1016/j.atmosres.2010.05.003.

Pruppacher, H., Klett, J., Springer, 1997. Microphysics of Clouds and Precipitation. Springer.

Qu, Y., Khain, A., Phillips, V., Ilotoviz, E., Shpund, J., Patade, S., Chen, B., 2020. The role of ice splintering on microphysics of deep convective clouds forming under different aerosol conditions: Simulations using the model with spectral bin microphysics. Journal of Geophysical Research: Atmospheres 125. URL:

http://dx.doi.org/10.1029/2019JD031312, doi: 10.1029/2019jd031312.

Qu, Z., Barker, H.W., Korolev, A.V., Milbrandt, J.A., Heckman, I., Bélair, S., Leroyer, S., Vaillancourt, P.A., Wolde, M., Schwarzenböck, A., Leroy, D., Strapp, J.W., Cole, J.N.S., Nguyen, L., Heidinger, A., 2018. Evaluation of a high-resolution numerical weather prediction model's simulated clouds using observations from cloudsat, goes-13 and in situ aircraft. Quarterly Journal of the Royal Meteorological Society 144, 1681–1694. URL: http://dx.doi.org/10.1002/qj.3318, doi: 10.1002/qj.3318.

Qu, Z., Korolev, A., Milbrandt, J.A., Heckman, I., Huang, Y., McFarquhar, G.M., Morrison, H., Wolde, M., Nguyen, C., 2022. The impacts of secondary ice production on microphysics and dynamics in tropical convection. Atmospheric Chemistry and Physics 22, 12287–12310. URL: http://dx.doi.org/10.5194/acp-22-12287-2022, doi: 10.5194/acp-22-12287-2022.

Sawada, M., Iwasaki, T., 2007. Impacts of ice phase processes on tropical cyclone development. Journal of the Meteorological Society of Japan. Ser. II 85, 479–494. URL: http://dx.doi.org/10.2151/jmsj.85.479, doi: 10.2151/jmsj.85.479.

Schwarzenboeck, A., Shcherbakov, V., Lefevre, R., Gayet, J.F., Pointin, Y., Duroure, C., 2009. Indications for stellar-crystal fragmentation in arctic clouds. Atmospheric Research 92, 220–228. URL: https://doi.org/10.1016/j.atmosres.2008.10.002, doi: 10.1016/j.atmosres.2008.10.002.

Seidel, J.S., Kiselev, A.A., Keinert, A., Stratmann, F., Leisner, T., Hartmann, S., 2024. Secondary ice production – no evidence of efficient rime-splintering mechanism. Atmospheric Chemistry and Physics 24, 5247–5263. URL: https://acp.copernicus.org/articles/24/5247/2024/, doi:

10.5194/acp-24-5247-2024.

Skamarock, W.C., Klemp, J.B., Dudhia, J., Gill, D.O., Liu, Z., Berner, J., Wang, W., Powers, J.G., Duda, M.G., Barker, D.M., Huang, X.Y., 2019. A description of the advanced research wrf model version 4 URL: https://opensky.ucar.edu/islandora/object/opensky:2898, doi: 10.5065/1DFH-6P97.

Sotiropoulou, G., Ickes, L., Nenes, A., Ekman, A.M.L., 2021a. Ice multiplication from ice–ice collisions in the high arctic: sensitivity to ice habit, rimed fraction, ice type and uncertainties in the numerical description of the process. Atmospheric Chemistry and Physics 21, 9741–9760. URL: http://dx.doi.org/10.5194/acp-21-9741-2021, doi: 10.5194/acp-21-9741-2021.

Sotiropoulou, G., Sullivan, S., Savre, J., Lloyd, G., Lachlan-Cope, T., Ekman, A.M.L., Nenes, A., 2020. The impact of secondary ice production on arctic stratocumulus. Atmospheric Chemistry and Physics 20, 1301–1316. URL: http://dx.doi.org/10.5194/acp-20-1301-2020, doi: 10.5194/acp-20-1301-2020.

Sotiropoulou, G., Vignon, E., Young, G., Morrison, H., O'Shea, S.J., Lachlan-Cope, T., Berne, A., Nenes, A., 2021b. Secondary ice production in summer clouds over the antarctic coast: an underappreciated process in atmospheric models. Atmospheric Chemistry and Physics 21, 755–771. URL: https://acp.copernicus.org/articles/21/755/2021/, doi: 10.5194/acp-21-755-2021.

Sullivan, S.C., Barthlott, C., Crosier, J., Zhukov, I., Nenes, A., Hoose, C., 2018. The effect of secondary ice production parameterization on the simulation of a cold frontal rainband.

Atmospheric Chemistry and Physics 18, 16461–16480. URL: https://acp.copernicus.org/articles/18/16461/2018/, doi: 10.5194/acp-18-16461-2018.

Takahashi, T., Nagao, Y., Kushiyama, Y., 1995. Possible high ice particle production during graupel–graupel collisions. Journal of the Atmospheric Sciences 52, 4523–4527. doi: 10.1175/1520-0469(1995)052<4523:phippd>2.0.co;2.

von Terzi, L., Neto, J.D., Ori, D., Myagkov, A., Kneifel, S., 2022. Ice microphysical processes in the dendritic growth layer: a statistical analysis combining multi-frequency and polarimetric doppler cloud radar observations. Atmospheric Chemistry and Physics 22, 11795–11821. URL: https://doi.org/10.5194/acp-22-11795-2022, doi: 10.5194/acp-22-11795-2022.

Thompson, G., Field, P.R., Rasmussen, R.M., Hall, W.D., 2008. Explicit forecasts of winter precipitation using an improved bulk microphysics scheme. part ii: Implementation of a new snow parameterization. Monthly Weather Review 136, 5095–5115. URL: http://dx.doi.org/10.1175/2008MWR2387.1, doi: 10.1175/2008mwr2387.1.

Tridon, F., Planche, C., Mroz, K., Banson, S., Battaglia, A., Van Baelen, J., Wobrock, W., 2019. On the realism of the rain microphysics representation of a squall line in the wrf model. part i: Evaluation with multifrequency cloud radar doppler spectra observations. Monthly Weather Review 147, 2787–2810. URL: http://dx.doi.org/10.1175/MWR-D-18-0018.1, doi: 10.1175/mwr-d-18-0018.1.

Vardiman, L., 1978. The generation of secondary ice particles in clouds by crystal–crystal collision. Journal of the Atmospheric Sciences 35, 2168–2180. URL:

https://doi.org/10.1175/1520-0469(1978)035<2168:tgosip>2.0.co;2, doi: 10.1175/1520-0469(1978)035<2168:tgosip>2.0.co;2.

Waman, D., Deshmukh, A., Jadav, A., Patade, S., Gautam, M., Phillips, V., Bansemer, A., Jakobsson, J., 2023. Effects from time dependence of ice nucleus activity for contrasting cloud types. Journal of the Atmospheric Sciences 80, 2013–2039. URL: https://doi.org/10.1175/jas-d-22-0187.1, doi: 10.1175/jas-d-22-0187.1.

Waman, D., Patade, S., Jadav, A., Deshmukh, A., Gupta, A.K., Phillips, V.T.J., Bansemer, A., DeMott, P.J., 2022. Dependencies of four mechanisms of secondary ice production on cloud-top temperature in a continental convective storm. Journal of the Atmospheric Sciences 79, 3375–3404. URL: https://doi.org/10.1175/jas-d-21-0278.1, doi: 10.1175/jas-d-21-0278.1.

Wang, P.K., Ji, W., 2000. Collision efficiencies of ice crystals at low–intermediate reynolds numbers colliding with supercooled cloud droplets: A numerical study. Journal of the Atmospheric Sciences 57, 1001–1009. URL: https://doi.org/10.1175/1520-0469(2000)057<1001:ceoica>2.0.co;2, doi: 10.1175/1520-0469(2000)057<1001:ceoica>2.0.co;2.

Young, G., Lachlan-Cope, T., O'Shea, S.J., Dearden, C., Listowski, C., Bower, K.N., Choularton, T.W., Gallagher, M.W., 2019. Radiative effects of secondary ice enhancement in coastal antarctic clouds. Geophysical Research Letters 46, 2312–2321. URL: http://dx.doi.org/10.1029/2018GL080551, doi: 10.1029/2018gl080551.

Zhao, X., Liu, X., 2021. Global importance of secondary ice production. Geophysical Research Letters 48. URL: http://dx.doi.org/10.1029/2021GL092581, doi: 10.1029/2021gl092581.

Zhao, X., Liu, X., Phillips, V.T.J., Patade, S., 2021. Impacts of secondary ice production on arctic mixed-phase clouds based on arm observations and cam6 single-column model simulations. Atmospheric Chemistry and Physics 21, 5685–5703. URL: http://dx.doi.org/10.5194/acp-21-5685-2021, doi: 10.5194/acp-21-5685-2021.

Ziegler, C.L., Ray, P.S., MacGorman, D.R., 1986. Relations of kinematics, microphysics and electrification in an isolated mountain thunderstorm. Journal of Atmospheric Sciences 43, 2098–2115.

Author statement
Pierre Grzegorczyk: Writing – review & editing, Writing – original draft, Visualization, Validation, Methodology, Investigation, Software, Formal analysis.
Wolfram Wobrock: Writing – review & editing, Writing – original draft, Software, Supervision, Validation, Methodology, Investigation, Conceptualization.
Antoine Canzi: Writing – original draft, Validation, Software, Formal analysis
Laurence Niquet: Writing – original draft, Validation
Frédéric Tridon: Writing – original draft, Validation
Céline Planche: Writing – review & editing, Writing – original draft, Conceptualization, Resources, Supervision, Project administration, Funding acquisition, Validation, Methodology, Investigation.

Declaration of interests
The authors declare that they have no known competing financial interests or personal relationships that could have appeared to influence the work reported in this paper.

Highlights

- Parameterizations of Hallett-Mossop, fragmentation of freezing drops, and fragmentation due to ice–ice collision are tested for deep convective cloud case, using a 3D bin micro-physics model
- Excluding SIP gives a large underestimation of small ice crystals for temperatures warmer than -30 °C
- Incorporating Hallett-Mossop and fragmentation due to ice–ice collision processes leads to

ice crystal number concentrations close to observed values

- Fragmentation of freezing drops affect minimally the properties of the cloud at its mature stage
- The size of fragments generated from fragmentation due to ice–ice collision significantly influences the shape of ice particle size distribution

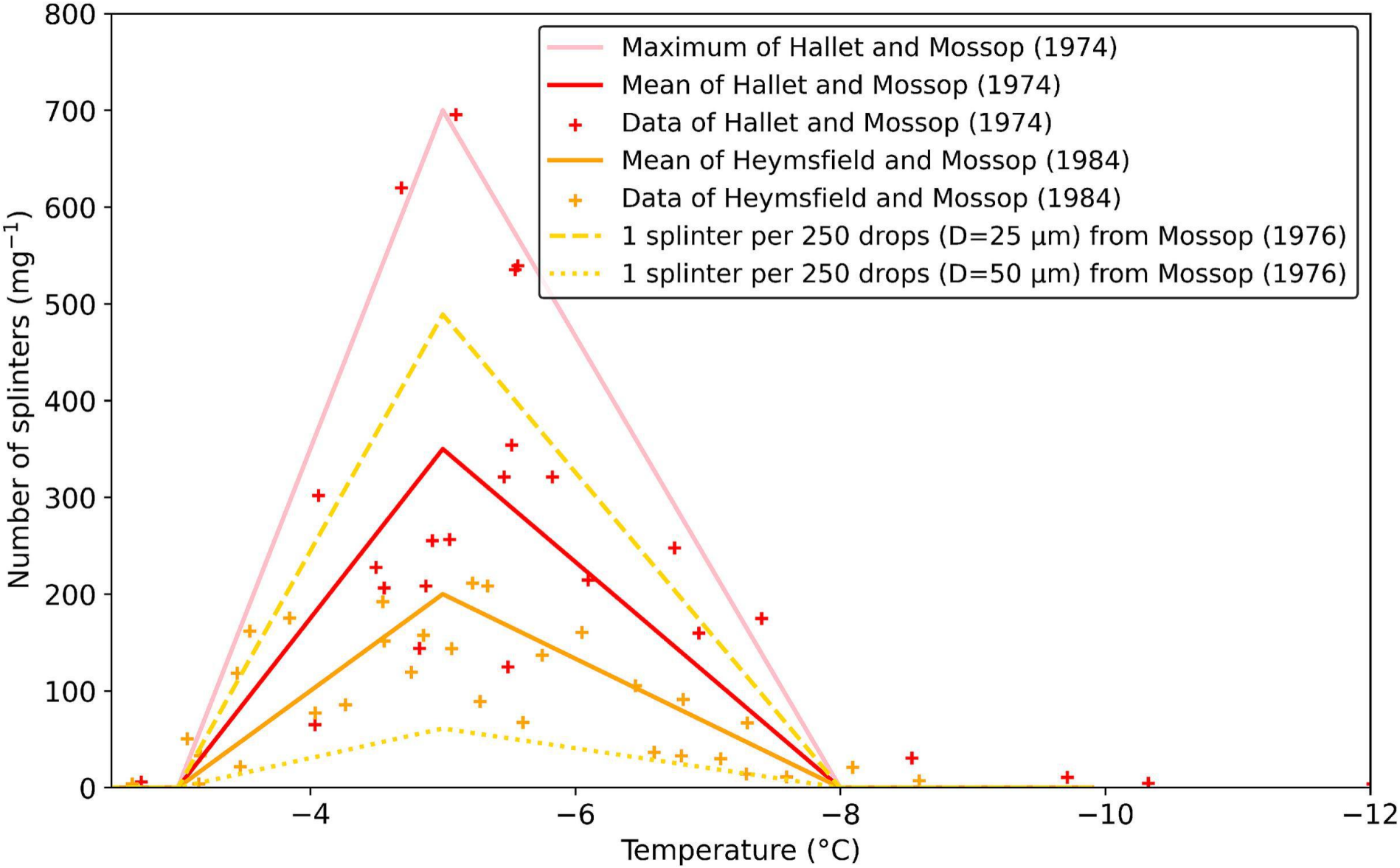
Maximum of Hallet and Mossop (1974)
Mean of Hallet and Mossop (1974)
Data of Hallet and Mossop (1974)
Mean of Heymsfield and Mossop (1984)
Data of Heymsfield and Mossop (1984)
1 splinter per 250 drops (D=25 µm) from Mossop (1976)
1 splinter per 250 drops (D=50 µm) from Mossop (1976)
Number of splinters (mg^{-1})
Temperature (°C)
800
700
600
500
400
300
200
100
0
−4
−6
−8
−10
−12

Figure 1

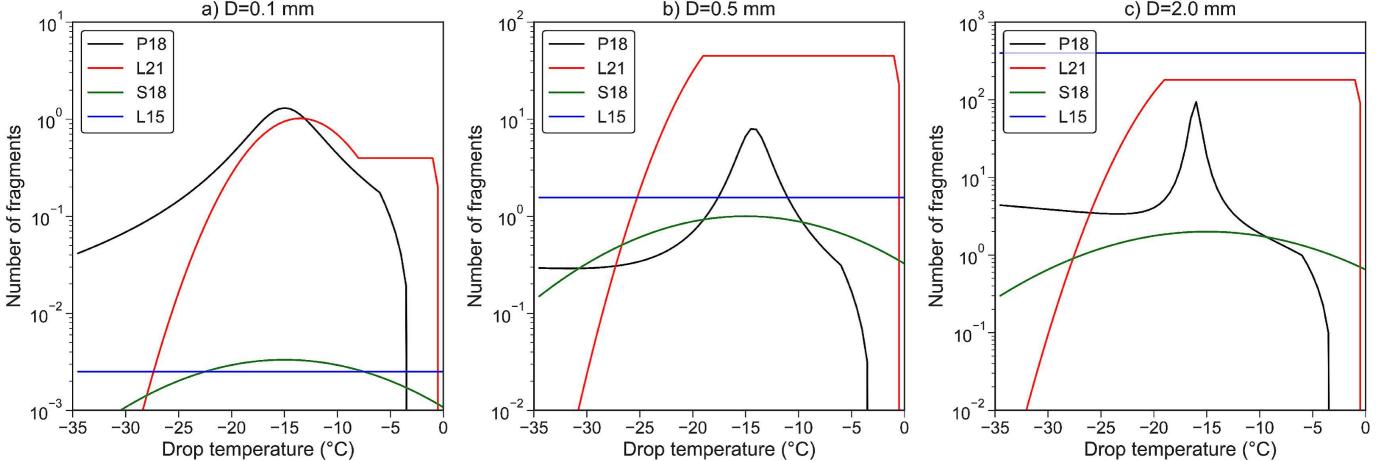
a) D=0.1 mm
b) D=0.5 mm
c) D=2.0 mm
P18
L21
S18
L15
Number of fragments
Drop temperature (°C)

Figure 2

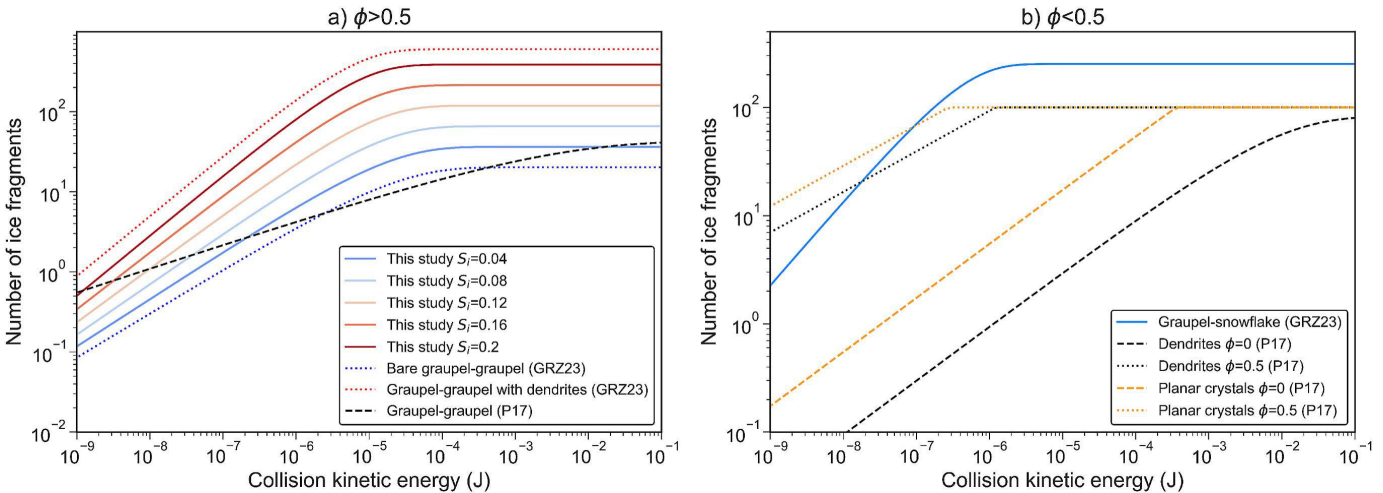
a) ϕ>0.5
Number of ice fragments
Collision kinetic energy (J)
This study S_i=0.04
This study S_i=0.08
This study S_i=0.12
This study S_i=0.16
This study S_i=0.2
Bare graupel-graupel (GRZ23)
Graupel-graupel with dendrites (GRZ23)
Graupel-graupel (P17)
b) ϕ<0.5
Number of ice fragments
Collision kinetic energy (J)
Graupel-snowflake (GRZ23)
Dendrites ϕ=0 (P17)
Dendrites ϕ=0.5 (P17)
Planar crystals ϕ=0 (P17)
Planar crystals ϕ=0.5 (P17)

Figure 3

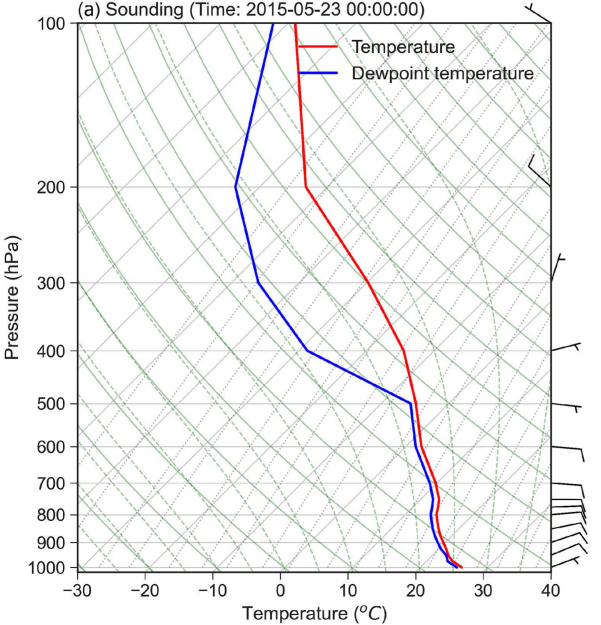
(a) Sounding (Time: 2015-05-23 00:00:00)
Temperature
Dewpoint temperature
Pressure (hPa)
100
200
300
400
500
600
700
800
900
1000
−30
−20
−10
0
10
20
30
40
Temperature (°C)

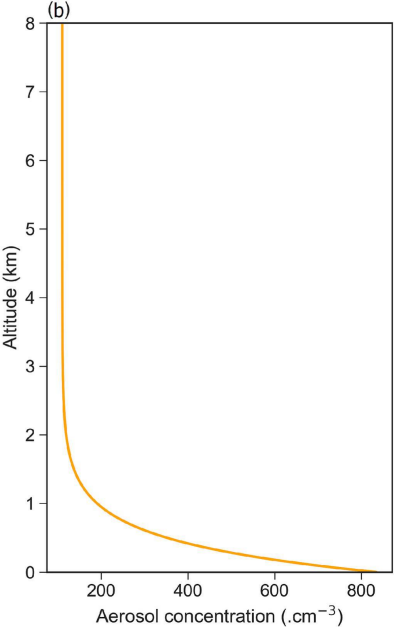
(b)
Altitude (km)
0
1
2
3
4
5
6
7
8
200
400
600
800
Aerosol concentration (.cm^{-3})

Figure 4

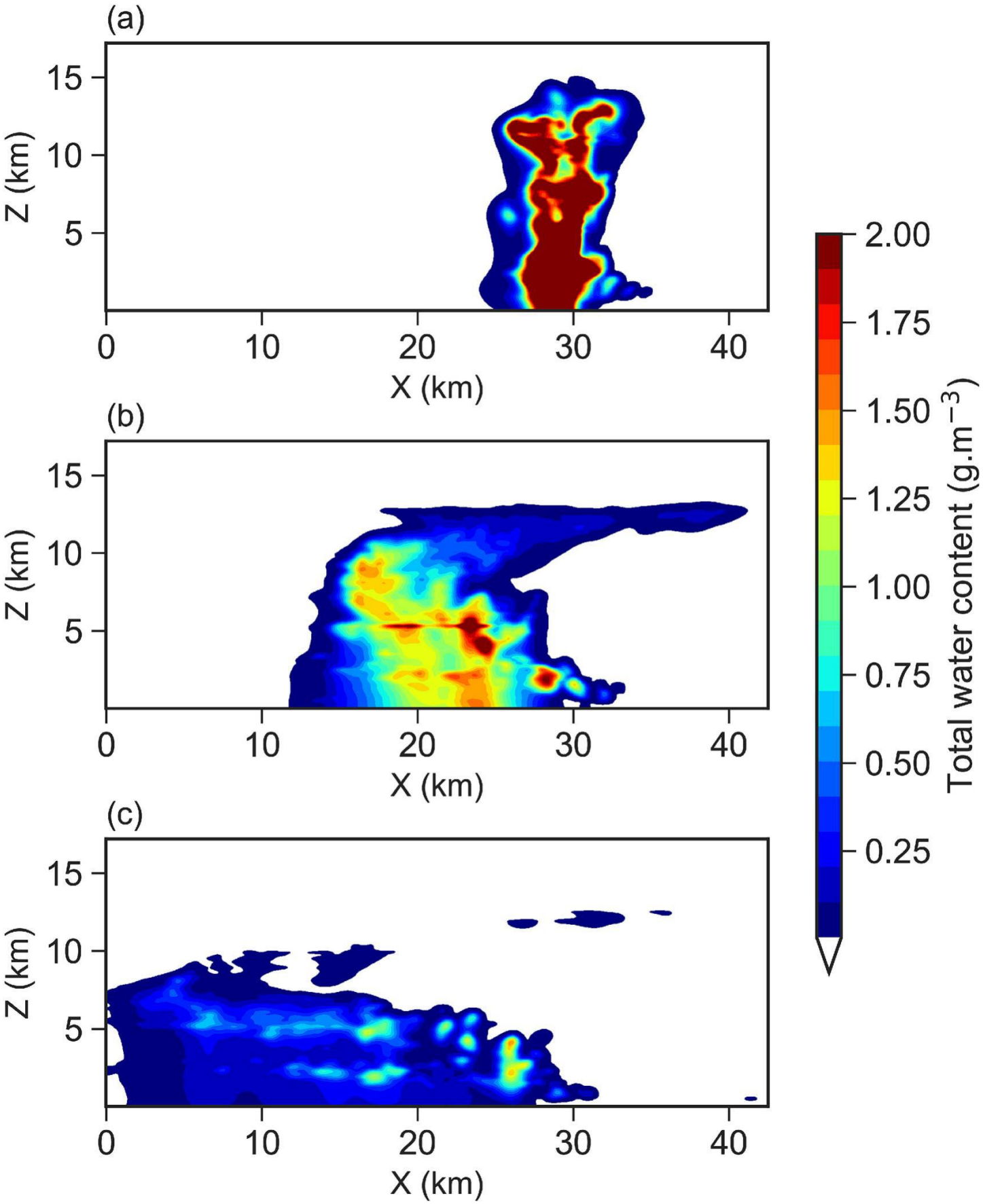
(a)
(b)
(c)
Z (km)
X (km)
0
10
20
30
40
5
10
15
2.00
1.75
1.50
1.25
1.00
0.75
0.50
0.25
Total water content (g.m^{-3})

Figure 5

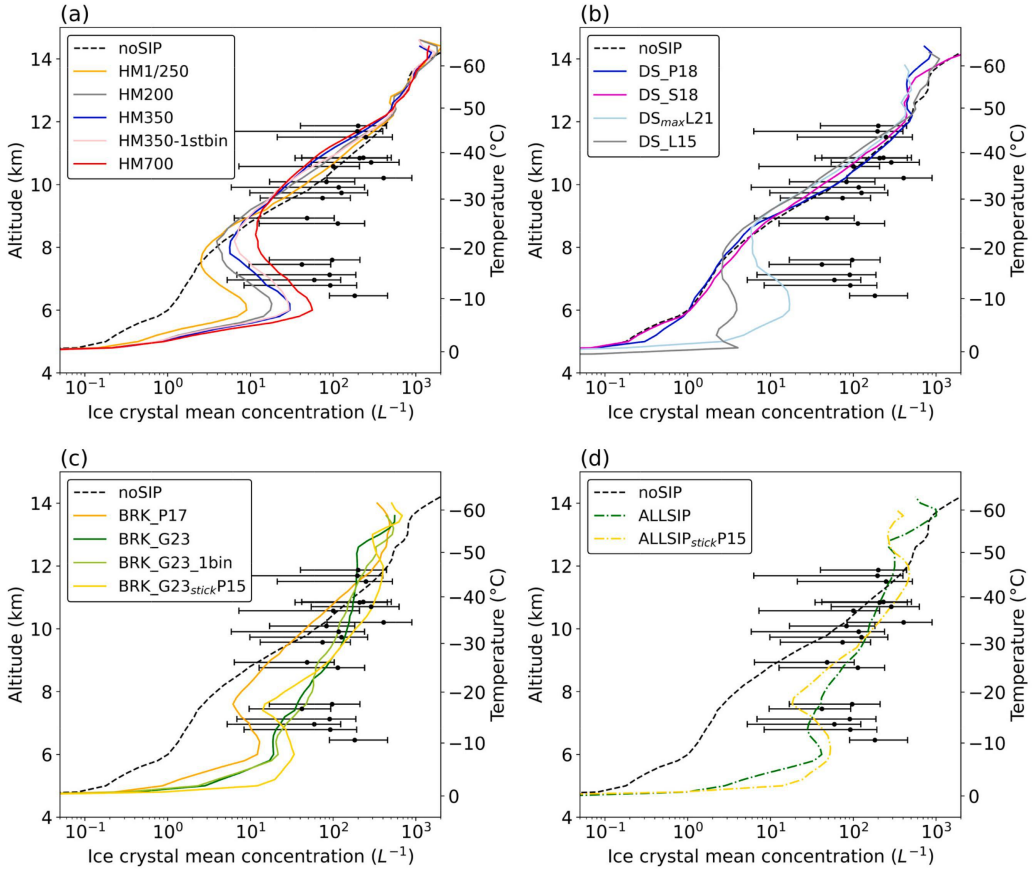
(a)
noSIP
HM1/250
HM200
HM350
HM350-1stbin
HM700
Altitude (km)
Temperature (°C)
Ice crystal mean concentration (L^{-1})
(b)
noSIP
DS_P18
DS_S18
DS$_{max}$L21
DS_L15
Altitude (km)
Temperature (°C)
Ice crystal mean concentration (L^{-1})
(c)
noSIP
BRK_P17
BRK_G23
BRK_G23_1bin
BRK_G23$_{stick}$P15
Altitude (km)
Temperature (°C)
Ice crystal mean concentration (L^{-1})
(d)
noSIP
ALLSIP
ALLSIP$_{stick}$P15
Altitude (km)
Temperature (°C)
Ice crystal mean concentration (L^{-1})

Figure 6

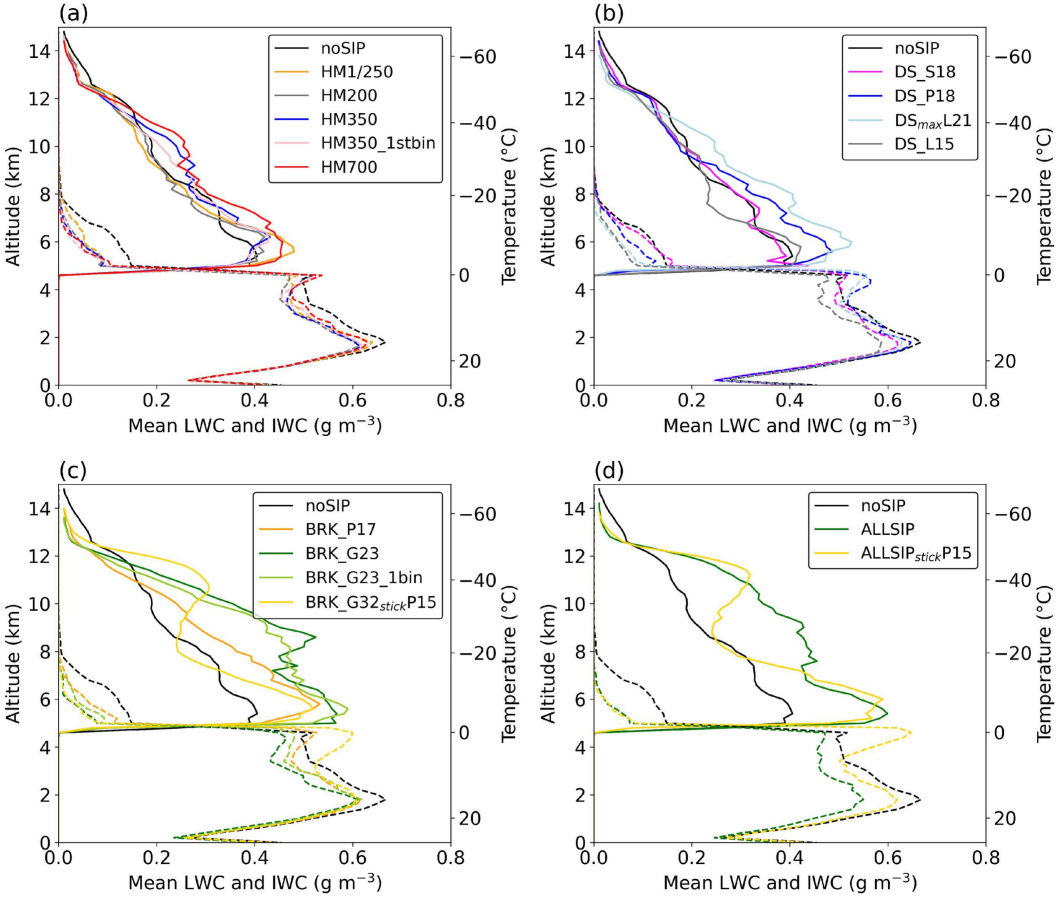
(a)
noSIP
HM1/250
HM200
HM350
HM350_1stbin
HM700
(b)
noSIP
DS_S18
DS_P18
DS$_{max}$L21
DS_L15
(c)
noSIP
BRK_P17
BRK_G23
BRK_G23_1bin
BRK_G32$_{stick}$P15
(d)
noSIP
ALLSIP
ALLSIP$_{stick}$P15
Altitude (km)
Temperature (°C)
Mean LWC and IWC (g m^{-3})

Figure 7

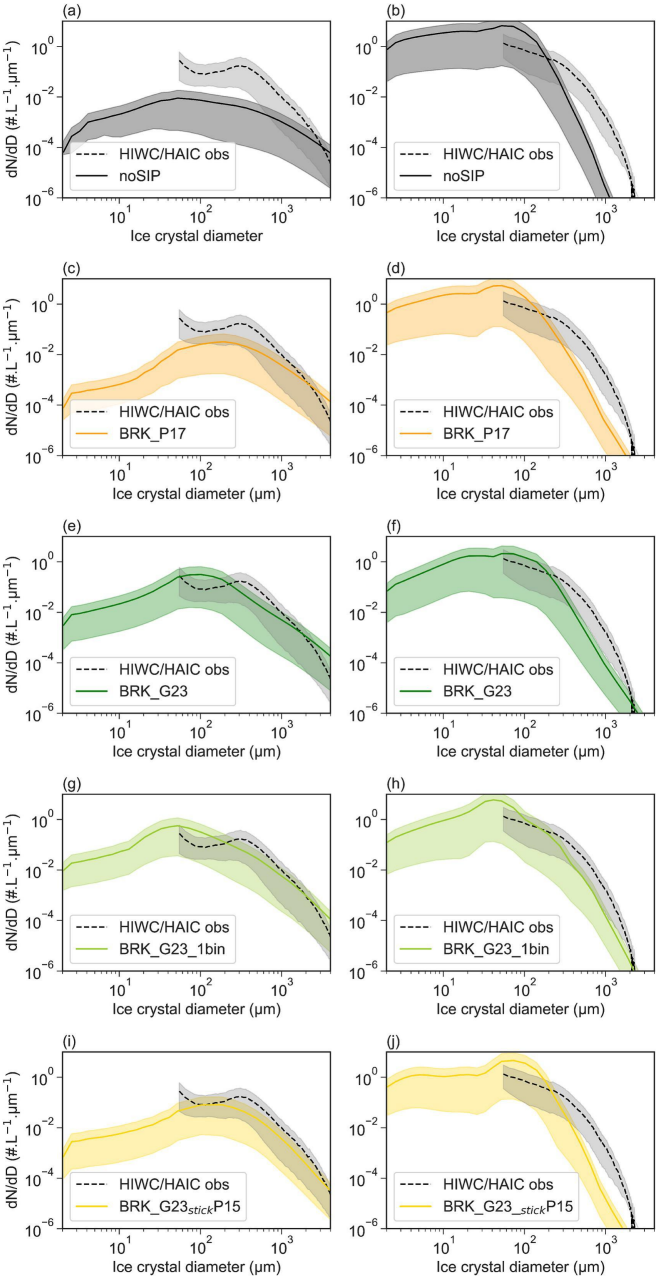
(a)
(b)
(c)
(d)
(e)
(f)
(g)
(h)
(i)
(j)
dN/dD (#.L^{-1}.µm^{-1})
Ice crystal diameter
Ice crystal diameter (µm)
HIWC/HAIC obs
noSIP
BRK_P17
BRK_G23
BRK_G23_1bin
BRK_G23$_{stick}$P15
BRK_G23_$_{stick}$P15

Figure 8

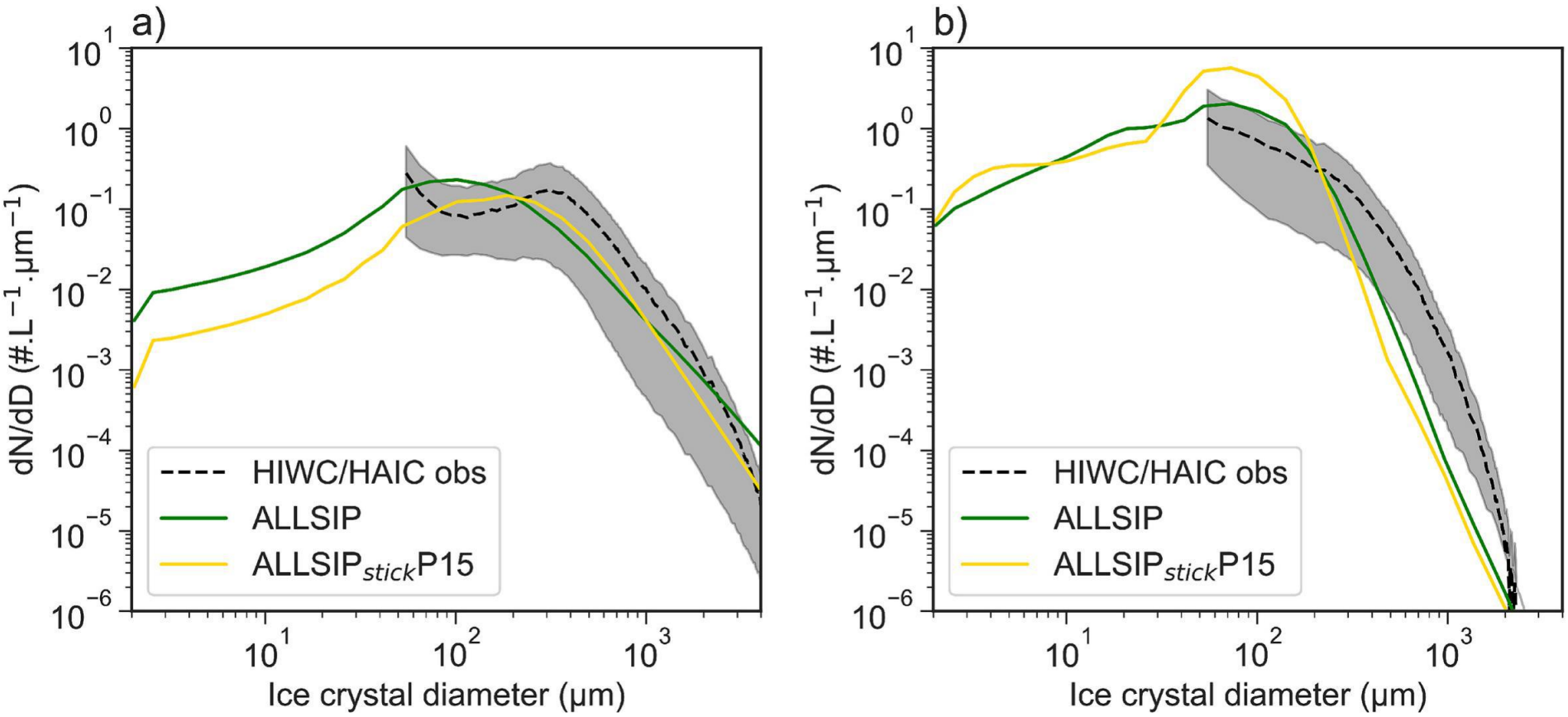
a)
b)
dN/dD (#.L^{-1}.µm^{-1})
Ice crystal diameter (µm)
HIWC/HAIC obs
ALLSIP
ALLSIP$_{stick}$P15

Figure 9